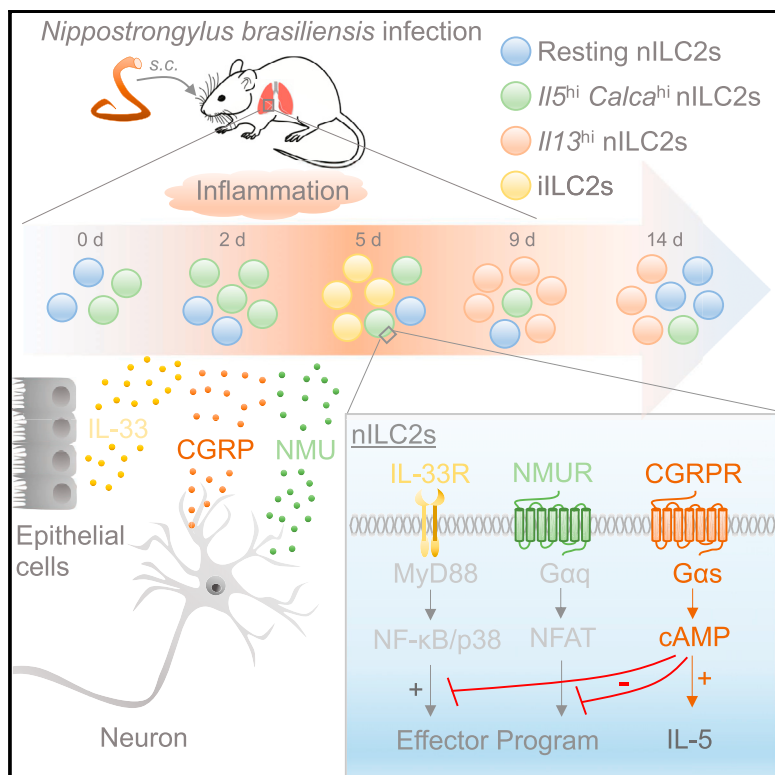


Immunity

Neuropeptide CGRP Limits Group 2 Innate Lymphoid Cell Responses and Constrains Type 2 Inflammation

Graphical Abstract



Authors

Hiroyuki Nagashima, Tanel Mahlakõiv, Han-Yu Shih, ..., Yuka Kanno, David Artis, John J. O'Shea

Correspondence

kannoy@mail.nih.gov (Y.K.), dartis@med.cornell.edu (D.A.), john.oshea@nih.gov (J.J.O.)

In Brief

Neuronal and immune systems coordinately orchestrate responses at mucosal barriers. Nagashima et al. applied scRNA-seq technology to track type 2 immune responses in worm infection, identifying neuropeptide CGRP as a factor that modulates inflammation. The study suggests that CGRP may be a useful target in type 2 inflammation.

Highlights

- Single-cell analysis reveals heterogeneity of ILC2 responses to *N. brasiliensis*
- Il5^{hi}*ILC2s express CGRP and its receptor following helminth infection
- CGRP modulates type 2 cytokine production by ILC2s induced by alarmin and NMU
- CGRP constrains the magnitude of innate type 2 responses following helminth infection

Neuropeptide CGRP Limits Group 2 Innate Lymphoid Cell Responses and Constrains Type 2 Inflammation

Hiroyuki Nagashima,^{1,8} Tanel Mahlaköiv,^{2,8} Han-Yu Shih,¹ Fred P. Davis,¹ Francoise Meylan,¹ Yuefeng Huang,^{3,7} Oliver J. Harrison,⁴ Chen Yao,¹ Yohei Mikami,¹ Joseph F. Urban, Jr.,⁵ Kathleen M. Caron,⁶ Yasmine Belkaid,⁴ Yuka Kanno,^{1,*} David Artis,^{2,*} and John J. O'Shea^{1,9,*}

¹Lymphocyte Cell Biology Section, Molecular Immunology and Inflammation Branch, National Institute of Arthritis, Musculoskeletal and Skin Diseases, NIH, Bethesda, MD 20892, USA

²Jill Roberts Institute for Research in Inflammatory Bowel Disease, Joan and Sanford I. Weill Department of Medicine, Department of Microbiology and Immunology, Weill Cornell Medicine, Cornell University, New York, NY 10021, USA

³Laboratory of Immune System Biology, National Institute of Allergy and Infectious Diseases, NIH, Bethesda, MD 20892, USA

⁴Metaorganism Immunity Section, Laboratory of Immune System Biology, National Institute of Allergy and Infectious Diseases, NIH, Bethesda, MD 20892, USA

⁵US Department of Agriculture, Agricultural Research Service, Beltsville Human Nutrition Research Center, Diet, Genomics, and Immunology Laboratory, Beltsville, MD 20705-2350, USA

⁶Department of Cell Biology and Physiology, University of North Carolina at Chapel Hill, Chapel Hill, NC 27599, USA

⁷Present address: Department of Microbiology and Immunology, Vagelos College of Physicians and Surgeons, Columbia University, New York, NY 10032, USA

⁸These authors contributed equally

⁹Lead contact

*Correspondence: kannoy@mail.nih.gov (Y.K.), dartis@med.cornell.edu (D.A.), john.oshea@nih.gov (J.J.O.)

<https://doi.org/10.1016/j.immuni.2019.06.009>

SUMMARY

Innate lymphocytes maintain tissue homeostasis at mucosal barriers, with group 2 innate lymphoid cells (ILC2s) producing type 2 cytokines and controlling helminth infection. While the molecular understanding of ILC2 responses has advanced, the complexity of microenvironmental factors impacting ILC2s is becoming increasingly apparent. Herein, we used single-cell analysis to explore the diversity of gene expression among lung lymphocytes during helminth infection. Following infection, we identified a subset of ILC2s that preferentially expressed *Iil5*-encoding interleukin (IL)-5, together with *Calca*-encoding calcitonin gene-related peptide (CGRP) and its cognate receptor components. CGRP in concert with IL-33 and neuromedin U (NMU) supported IL-5 but constrained IL-13 expression and ILC2 proliferation. Without CGRP signaling, ILC2 responses and worm expulsion were enhanced. Collectively, these data point to CGRP as a context-dependent negative regulatory factor that shapes innate lymphocyte responses to alarmins and neuropeptides during type 2 innate immune responses.

INTRODUCTION

The vertebrate immune system comprises innate and adaptive arms that use distinct modalities to perceive and respond to microbial insults. The former employs genetically conserved, hardwired pathogen recognition receptors, whereas the latter

employs clonotypic antigen receptors generated by DNA rearrangement. More recently, the innate lymphoid cell (ILC) family has been identified and shown to act in concert with conventional T and B cells to orchestrate host defense, barrier integrity, homeostasis, and tissue repair (Artis and Spits, 2015; Diefenbach et al., 2014; Eberl et al., 2015; Morita et al., 2016; Sonnenberg and Artis, 2015; Spits and Cupedo, 2012).

The major difference between ILCs and T helper (Th) cells is their readiness to produce effector cytokines prior to encountering microbial pathogens (Robinette et al., 2015; Shih et al., 2016). While ILC precursors acquire their distinct accessibility of regulatory elements to drive cytokine expression in a developmental, stepwise fashion, naive Th cells exhibit markedly “inactive” chromatin landscapes at effector loci and dramatically acquire accessibility only after activation and final differentiation. This implies that tissue ILCs are conditioned via microenvironmental factors to rapidly respond to local demands in the tissue in which they reside.

Indeed, these tissue-specific environmental signals have a substantial impact on lymphocyte gene expression profiles beyond lineage per se (Rankin and Artis, 2018). Recently, many reports point to neural regulation of local immune responses at barrier tissues where lymphocytes reside in close proximity to dense neuronal networks. For example, ILC2s in the mouse gastrointestinal tract co-localize with cholinergic neurons that express the neuropeptide neuromedin U (NMU) and selectively express the NMU receptor 1 (NMUR1) (Cardoso et al., 2017; Klose et al., 2017; Wallrapp et al., 2017). Acting with the alarmin interleukin (IL)-33 and IL-25, NMU induces ILC2 proliferation and secretion of the type 2 cytokines and promotes lung inflammation or expulsion of the gastrointestinal nematode *Nippostrongylus brasiliensis*. Engagement of the β-adrenergic receptor on ILC2s counteracts ILC2 activation induced by helminth and fungi, serving as a cell-intrinsic negative

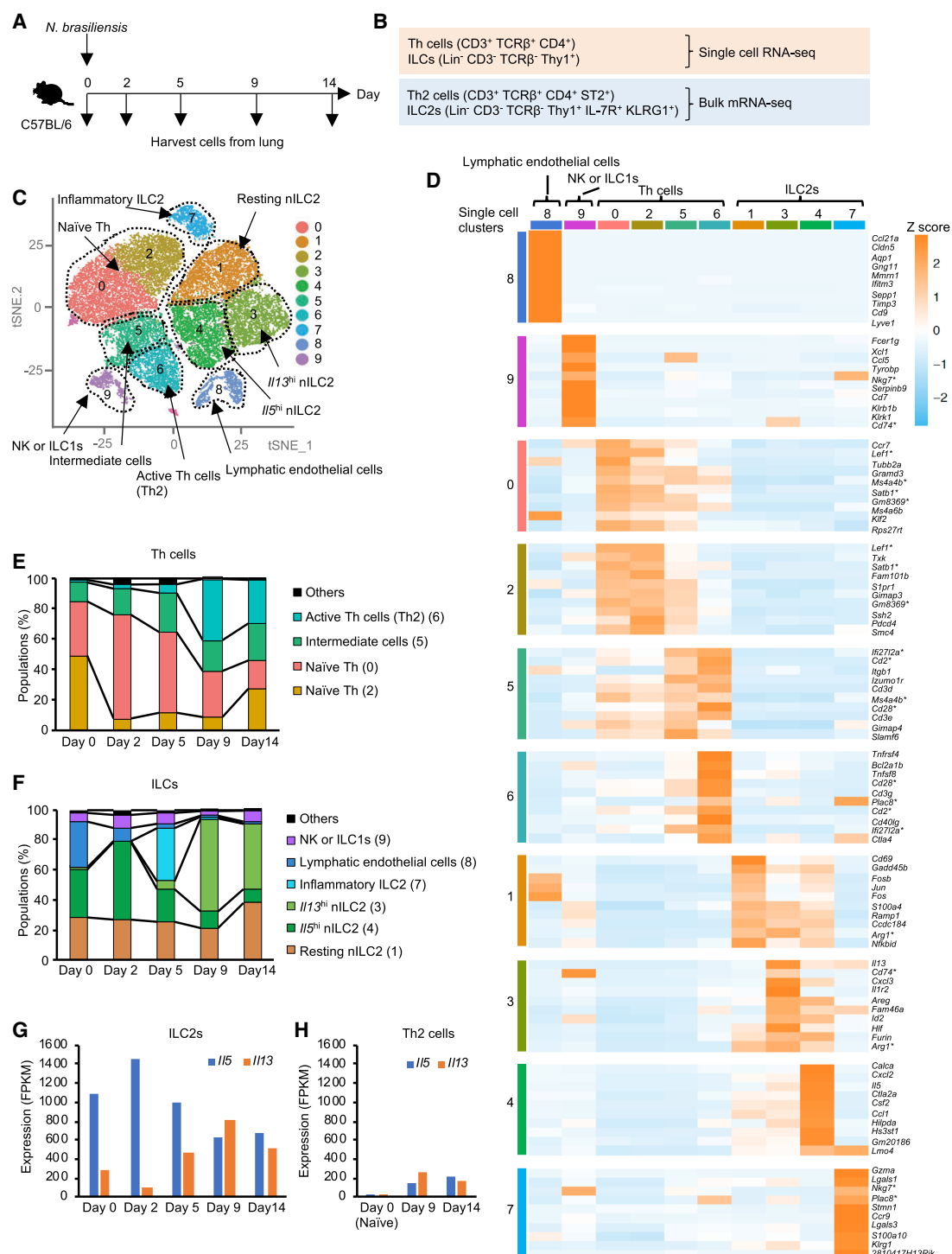


Figure 1. Diverse Populations of Lung ILCs and T Helper Cells Emerge during Helminth Infection

(A and B) Experimental design for single-cell RNA-seq (scRNA-seq) and bulk mRNA-seq of Th cells and ILCs from lungs of *N. brasiliensis*-infected mice. Time course of *N. brasiliensis* infection experiment (A) and cell markers (B) for isolating total Th cells and total ILCs for scRNA-seq or Th2 cells and ILC2s for bulk mRNA-seq.

(C) Ten gene expression clusters (0–9) projected on the t-distributed stochastic neighbor embedding (tSNE) plot of the scRNA-seq libraries from mice during *N. brasiliensis* infection as in (A). Clusters, depicted by color, were identified by Seurat based on gene expression profiles in an unbiased manner, with manually labeling inferred cluster “identities.” For additional details, see Figures S1E–S1J.

(legend continued on next page)

regulator of ILC2 responses (Moriyama et al., 2018). These emerging findings of neural-immune crosstalk are collectively referred to as neuroimmune cell units (Veiga-Fernandes and Pachnis, 2017).

One such neuropeptide reported to regulate immune cells is α -CGRP (α -calcitonin gene-related peptide), a 37-amino-acid neuropeptide produced as an alternatively spliced product of the calcitonin (*Calca*) gene (Holzmann, 2013; Russell et al., 2014). Secreted by pulmonary neuroendocrine cells (PNECs) in the lung, CGRP exacerbates experimentally induced asthma in mice via production of IL-5 in ILC2s (Sui et al., 2018). In contrast, CGRP produced by nociceptor neurons, termed transient receptor potential vanilloid (TRPV)1⁺ neurons, attenuates severity of *Staphylococcus aureus*-induced pneumonia by limiting neutrophils and $\gamma\delta$ T cells in the lung (Baral et al., 2018). These results argue for both pro- and anti-inflammatory effects of CGRP on immune responses in the lung depending on the context of inflammation.

In the present study, we examined dynamic transcriptomic programs of lung lymphocytes during helminth infection using single-cell RNA sequencing (scRNA-seq) to decipher microenvironmental signals received by lymphocytes. This analysis revealed that multiple subsets of innate and adaptive lymphocytes emerged with different kinetics during infection, including subsets of ILCs that preferentially expressed IL-5 versus IL-13. We identified the expression of the neuropeptide CGRP (*Calca*) and its cognate receptor enriched within an $II5^{hi}$ subpopulation of ILC2s. CGRP, which mediated cyclic AMP (cAMP) production, antagonized many of the actions of NMU and IL-33 such as promotion of cell proliferation and IL-13 production, while selectively promoting IL-5 production. Without CGRP signaling, ILC2 responses were enhanced, facilitating worm expulsion *in vivo*. Collectively, CGRP is a crucial factor that coordinately shapes the magnitude and complexity of type 2 innate response with other tissue signals. The complex interplay among neuropeptides, alarmin, and cytokines may well be relevant to the clinical use of CGRP antagonists and could offer insights into therapeutic opportunities.

RESULTS

Diverse Populations of Lung ILCs and Th Cells Emerge during Helminth Infection

To gain insights into the type 2 responses developing during a model helminth infection, we inoculated mice with infective *N. brasiliensis* larvae, collected multiple fractions of Th cells (CD3⁺ TCR β ⁺ CD4⁺) and ILCs (Lin⁻ CD3⁻ TCR β ⁻ Thy1⁺) from the lung, and analyzed gene expression by scRNA-seq. We also analyzed gene expression from pooled populations of Th2 cells (CD3⁺ TCR β ⁺ CD4⁺ ST2⁺) and ILC2s (Lin⁻ CD3⁻ TCR β ⁻ CD4⁻ Thy1⁺ CD127⁺ KLRG1⁺) from the same mice (Figures 1A–1B and S1A–S1D) in which approximately 90% of ST2⁺ Th cells were transcription factor GATA3^{hi} Foxp3⁻ Th2 cells (Fig-

ure S1B). For single-cell data, we aggregated all data points (Figure S1E) and identified ten clusters in an unbiased manner based on differentially expressed genes (DEGs) (Figure 1C) and inferred cluster identities based on DEGs and marker gene expression (Figures 1C, 1D, and S1F–S1J; Table S1). For Th clusters, two overlapping populations of naive T cells could be discerned (C0, C2), and a distinct population of active Th2 cells was readily apparent (C6). A population of T cells with transcriptomes shared by both naive and active Th2 cells was noted and designated as “intermediate” cells (C5). Analysis of ILC populations revealed two different ILC2 populations: natural ILC2 (nILC2) (C1, C3, and C4) defined as *Il1rl1* (ST2)⁺ KLRG1^{low} ILC2 and inflammatory ILC2 (iILC2) (C7) defined as ST2⁻ KLRG1^{hi} ILC2 (Figures 1D and S1F) (Huang et al., 2015). nILC2s were further classified into resting (C1), *Il13*^{hi} (C3), and *Il5*^{hi} (C4) cells. The proportion of the different populations varied during the course of *N. brasiliensis* infection. While the naive clusters declined, the active Th2 cell population peaked at day 9 and lasted until day 14 (Figure 1E). By contrast, nILC2 expressed the type 2 cytokine IL-5 at steady state; more than 50% of nILC2 were *Il5*^{hi} cells. Following infection, *Il5*^{hi} nILC2s increased, peaking early on day 2. This was followed by transient emergence of iILC2 (day 5) and later, expansion of *Il13*^{hi} cells (day 9) (Figures 1F and 1G). The dynamic transition of ILC2 subpopulations and the differential time course of *Il5* and *Il13* expression measured by scRNA-seq was in line with previous studies using cytokine reporter mice (Huang et al., 2015; Ricardo-Gonzalez et al., 2018). Following infection, the proportion of innate versus adaptive populations of type 2 lymphoid cells shifted, with Th2 cells becoming dominant at day 9 (Th2: $\sim 2 \times 10^5$ cells, ILC2s: $\sim 3 \times 10^4$ cells) (Figures 1G, 1H, S1C and S1D). Furthermore, lung cell preparations included lymphatic endothelial cells (Shinoda et al., 2016) (C8) and NK or ILC1 (C9) (Figures S1I and S1J). Collectively, our single-cell analysis reveals a heterogeneous type 2 immune response and dynamic transitions both in ILCs and Th cells during helminth infection.

CGRP and Its Cognate Receptor Are Induced in ILC2s during Helminth Infection

Seven transmembrane (7TM) receptors are a large class of molecules whose ligands have profound effects on ILCs (Rankin and Artis, 2018). Using bulk mRNA-seq data, we evaluated the expression of 7TM receptors that might be relevant to the regulation of ILC2s, including receptors for chemokines, lipid metabolites, and neuropeptides (Figure S2A). *Nmur1* and *Calcr1* encode neuropeptide receptors NMUR1 and calcitonin receptor-like receptor (CLR), whose ligands, NMU and CGRP, respectively, have been reported to promote ILC2 activation (Cardoso et al., 2017; Klose et al., 2017; Sui et al., 2018; Wallrapp et al., 2017). CLR forms a heterodimer with an accessory protein Ramp1, and *Calcr1* and *Ramp1* genes were expressed in nILC2 clusters (C1, C3, C4) but not in inflammatory ILC2s (C7), whereas *Nmur1* was minimally detectable at single-cell level (Figure 2A).

(D) Gene expression heatmap showing unbiased generation of top ten differentially expressed genes for each cluster. Genes picked for multiple clusters are marked with asterisk.

(E and F) Proportion of each cluster in the scRNA-seq library of Th cells (E) or ILCs (F) during the course of infection (days 0–14).

(G and H) Expression of *Il5* and *Il13* evaluated by bulk mRNA-seq in ILC2s (G) and naive Th cells and Th2 cells (H) isolated as shown in (B).

Data are from one experiment. See also Figure S1 and Table S1.

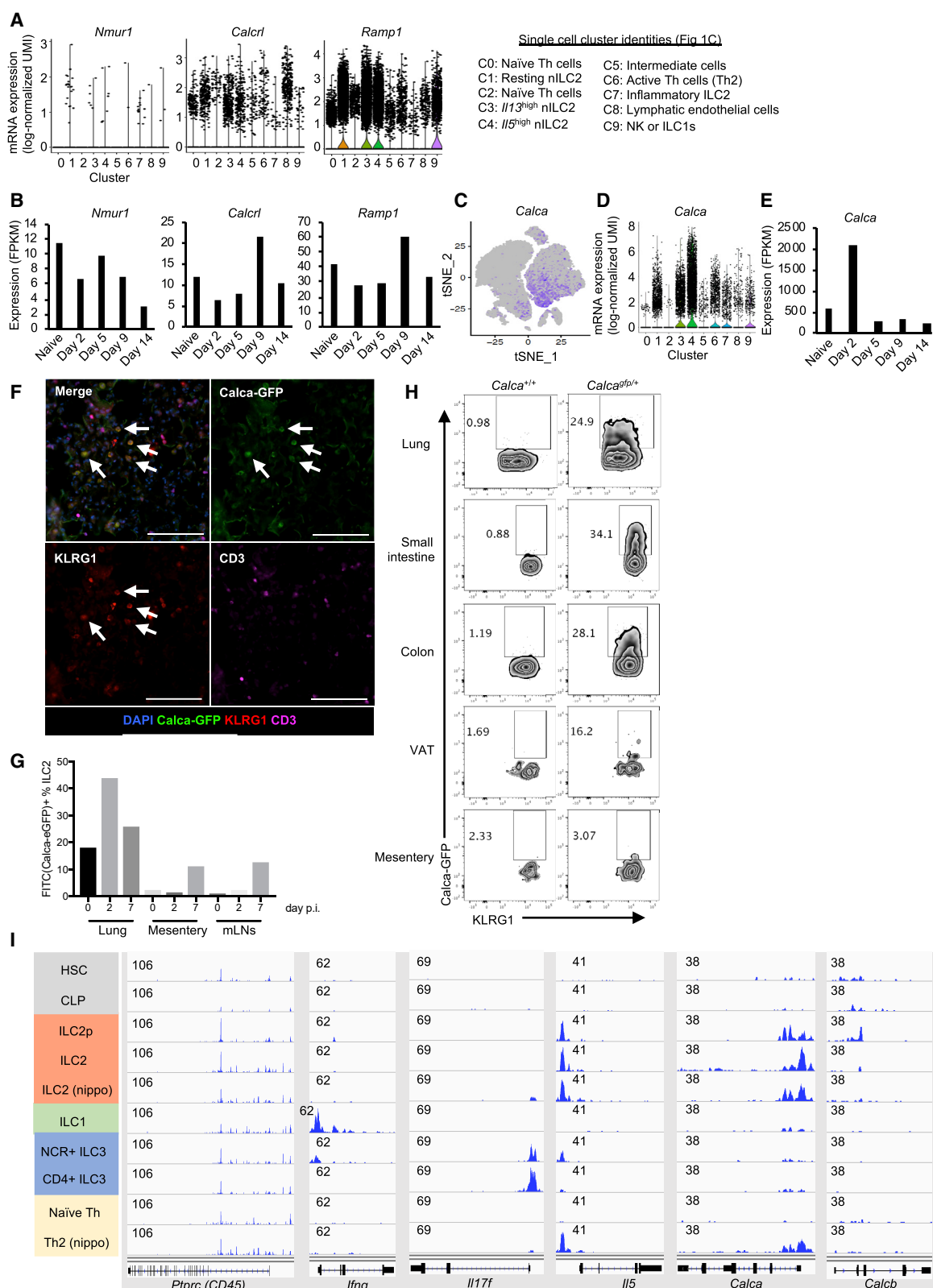


Figure 2. CGRP and Its Cognate Receptor Are Induced in ILC2s during Helminth Infection

(A) Single-cell expression of receptors for NMU and CGRP in each cell cluster defined as in Figure 1C.

(B) Kinetics of gene expression during *N. brasiliensis* infection in ILC2s for genes encoding receptors for NMU and CGRP using bulk mRNA-seq as in Figure 1B.

(legend continued on next page)

CGRP receptor (*Calcr1* and *Ramp1*) expression increased at a later time point following infection (day 9), whereas *Nmur1* expression in ILC2s was downregulated (Figure 2B).

Not only did we observe the regulated expression of CLR and Ramp1, we also found that the gene encoding CGRP (*Calca*), the ligand for this receptor, was highly expressed and dynamically regulated in ILC2s. At single-cell levels, *Calca* was enriched in *Il5^{hi}* ILC2 (C4) and to a lesser extent in activated Th2 cell fraction (C6) and in other ILC2 clusters (C1 and C3) (Figures 1D and 2C, and 2D). With bulk mRNA-seq, we confirmed high expression of *Calca* mRNA (~500 FPKM [fragments per kilobase of transcript per million mapped reads]) even in steady-state ILC2s and peaking at day 2 after infection (~2,000 FPKM). *Calca* expression waned quickly thereafter (Figure 2E), mirroring *Il5* transcription more closely than *Il13* (Figures 1D and 1F–1G).

Using *Calca* reporter mice, we evaluated populations of hematopoietic cells expressing *Calca* *in vivo*. Approximately 50% of *Calca*-expressing cells were ILC2s in the lung in the steady state; although other non-ILC2 populations (e.g., TCR β^+ T cells) were detected within GFP-positive cells (Figure S2B). *Calca* expression in ILC2s was further upregulated by intranasal administration of IL-33 or *N. brasiliensis* infection (Figures 2F, 2G, S2C, and S2D). ILC2s from tissues other than the lung also expressed *Calca* including the small intestine, colon, and visceral adipose tissue (VAT). *Calca* expression was barely detectable in mesenteric ILC2s (Figure 2H), indicating that *Calca* expression in ILC2s is differentially controlled in a tissue-specific manner.

To gain insight into regulation of the *Calca* gene, we analyzed prior assay for transposase-accessible chromatin using sequencing (ATAC-seq) data generated by our group (Shih et al., 2016) to evaluate accessibility of the *Calca* locus during ILC2 development or in *N. brasiliensis*-infected Th2 cells. The *Calca* locus acquired accessibility at the ILC2 precursor stage similar to *Il5* but was inaccessible in ILC1s, ILC3s, and naive T cells (Figure 2I). The *Calca* locus became accessible in Th2 cells induced by *N. brasiliensis* infection. The results indicate that *Calca* expression is selectively regulated in type 2 immune cells; as with other ILC loci, accessibility occurs in a developmental manner prior to acute activation in ILC2.

CGRP and NMU Have Divergent Effects on ILC2 Gene Expression

To evaluate the functional outcome of neuropeptide signaling, we stimulated isolated lung ILC2s with the alarmin IL-33 alone or in combination with NMU or CGRP and assessed IL-5 and IL-13 proteins by flow cytometry (Figures 3A and 3B). NMU cooperatively enhanced IL-5 and IL-13 expression with IL-33. On the other hand, CGRP exerted contrasting effects on IL-5 and IL-13, enhancing IL-5 and repressing IL-13 production mediated by IL-33. These results are in line with scRNA-seq data showing differential expression of IL-5 and IL-13 in ILC2s

following helminth infection (Figures 1C–1G), suggesting that CGRP may take part in controlling cytokine expression *in vivo*.

To gain a more comprehensive view of the direct effects of CGRP and other factors on ILC2, we treated isolated lung ILC2s *in vitro* with neuropeptides and IL-33 and assessed transcriptomic changes using mRNA-seq (Figures 3C–3F). IL-33, NMU, and CGRP had very distinct global impacts on transcriptomic output (Figure 3C), with a total of 958 genes being differentially regulated by IL-33, CGRP, and NMU, classified into four groups based on expression profiles (Figure 3D; Table S2). In line with the reported ability of CGRP to activate ILC2s (Sui et al., 2018), we identified 116 genes that were selectively induced by CGRP (group 3). On the other hand, a suppressive action of CGRP was also evident on genes otherwise induced by NMU and IL-33 (97 and 265 genes in groups 1 and 4, respectively). We also identified a group of 350 genes whose expression was higher before stimulation and downregulated with each stimulation tested (group 2).

We next analyzed the combinatorial effects of CGRP, NMU, and IL-33 on effector cytokines in more detail (Figure 3F). We found that while CGRP inhibited *Il2*, *Il9*, *Il4*, *Il6*, and *Il13* expression induced by IL-33 or IL-33+NMU, CGRP enhanced *Il5* in combination with IL-33 (Figure 3F), consistent with discordant regulation of IL-5 and IL-13 protein by CGRP (Figures 3A and 3B). *Areg* was another gene strongly induced with IL-33+CGRP, and it was further enhanced by addition of NMU (Figure 3F).

Since CGRP has previously been reported to inhibit T cell proliferation (Umeda et al., 1988), we tested the effects of IL-33, CGRP, and NMU on ILC2 proliferation. Whereas the combination of IL-33 and NMU strongly induced proliferation, CGRP suppressed proliferation induced by IL-33 and the combination of IL-33 and NMU with both *in vitro*-expanded ILC2 (Figures 3G and S3A) and fresh *ex vivo* ILC2 (Figure S3B). Even though CGRP induced IL-5 on a per-cell basis (Figures 3A–3B and 3F), the total amount of IL-5 in supernatants of cultures of ILC2s (5 day) was reduced by CGRP because of its anti-proliferative effect (Figure 3H); this was also the case for amphiregulin (Figure 3I). Although NMU did not induce *Areg* mRNA in the setting of short stimulation (4 h), 5 days culture with NMU strongly enhanced production of amphiregulin protein, suggesting that NMU elicited indirect positive control over *Areg* through induction of several STAT5 transcription factor-activating cytokines such as IL-2 and IL-9, all of which strongly enhance type 2 cytokine expression (Figures 3F and 3I) (Moro et al., 2010; Wilhelm et al., 2011). Notably, CGRP strongly induced *Calca* transcript compared with IL-33 alone. Moreover, NMU promoted the expression of CGRP receptor components (*Calcr1* and *Ramp1*), whereas it negatively regulated its own receptor, *Nmur1* (Figure 3J), consistent with the *in vivo* observation during *N. brasiliensis* infection (Figure 2B). Collectively, our data

(C–E) *Calca* expression in Th cells and ILCs using scRNA-seq (C and D, respectively) and confirmation by bulk mRNA-seq (E), as in (A) and (B).

(F) Immunohistochemical staining of lungs from *Calca*^{+/gfp} mice 7 days after *N. brasiliensis* infection. The arrows depict ILC2s (CD3⁺KLRG1⁺) that express *Calca* (GFP⁺). Scale bar, 100 μ m.

(G) *Calca* expression in ILC2s from lung, mesentery, and mesenteric LNs (mLNs) of *Calca*^{+/gfp} mice before (0) and after *N. brasiliensis* infection (days 2 and 7).

(H) *Calca*-driven expression of GFP in ILC2s from indicated tissues of *Calca*^{+/gfp} mice, assessed by flow cytometry.

(I) Accessibility of indicated loci in various cell types, as measured by ATAC-seq (data from Shih et al., 2016, GEO: GSE77695).

Data are from one experiment (A–E) or representative from three independent experiments with similar results (F–H). See also Figure S2.

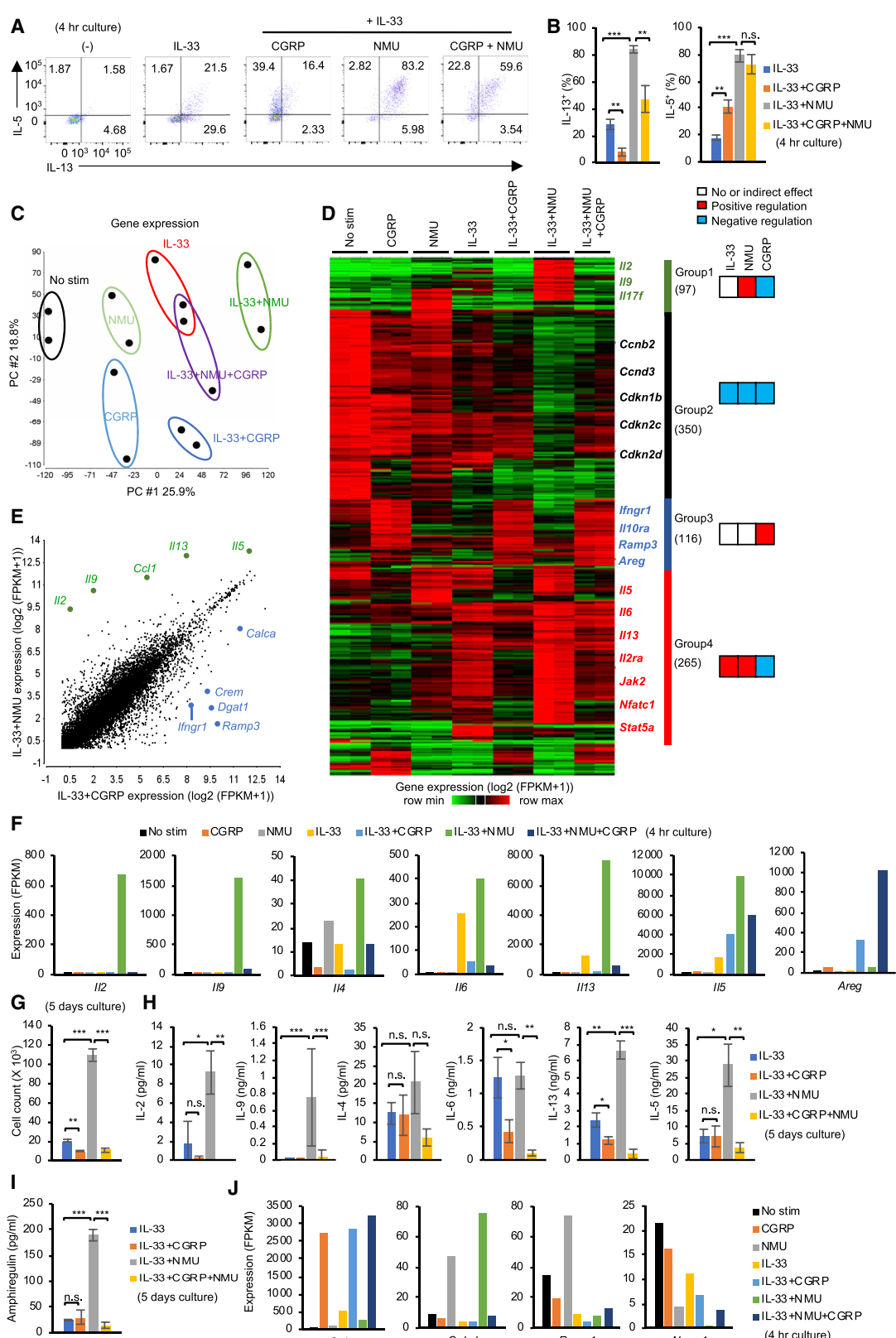


Figure 3. Differential Effects of CGRP and NMU on ILC2 Gene Expression

(A) Flow cytometric assessment of intracellular IL-5 and IL-13 expression in lung ILC2s in the absence of stimulation (-) or following stimulation with IL-33 alone, or in combination with CGRP or NMU for 4 h with inclusion of Brefeldin A.

(legend continued on next page)

indicate that NMU is a robust activator of ILC2 proliferation that cooperatively activates gene expression with IL-33 and especially impacts pro-inflammatory cytokines including IL-2, IL-6, IL-13, and IL-17F. In contrast, CGRP counteracts NMU by suppressing cell proliferation and gene expression of inflammatory cytokines. At the same time, CGRP dominantly activates a select gene module including *Il5* and *Areg*, leading to a unique type 2 cytokine expression profile in ILC2s.

CGRP and NMU Have Differential Effects on ILC2 Regulatory Elements

Having observed differential actions of CGRP and NMU on ILC2 gene expression and cytokine production, we next evaluated how genomic regulatory elements were controlled by these two neuropeptides using ATAC-seq (Figure 4). More than half of accessible regions (57% of peaks) were present before stimulation, but a large fraction of peaks (43%) were induced by neuropeptide or alarmin stimulation. Similar fractions (~10% of peaks) were uniquely affected by CGRP or NMU (Figure 4A). We next examined the frequency of opposing or independent actions of CGRP and NMU on chromatin accessibility (Figure 4B). We found that more NMU-induced peaks were suppressed by CGRP ($n = 4,390$ peaks, cluster A in Figure 4B) than the converse, i.e., CGRP-induced peaks suppressed by NMU ($n = 2,291$ peaks, cluster C). Under the conditions employed, this is consistent with a dominant effect of CGRP in counteracting the effect of NMU on transcription (Figure 3D).

Given the opposing regulation of *Il5* and *Il13* by CGRP and NMU (Figures 2A, 2B, and 2F), we examined the extended type 2 cell-associated cytokine loci for chromatin-accessible regions. Individually, IL-33 and the neuropeptides had minor effects on *Il5* and *Il13*, whereas the combination of IL-33 and NMU increased accessibility of both loci (Figure 4C). In contrast, the combination of IL-33 and CGRP selectively increased accessibility of *Il5* without impacting *Il13*. Moreover, the combination of IL-33, NMU, and CGRP reduced *Il13* accessibility while preserving *Il5* accessibility, in line with transcript or protein expression data for the two cytokines (Figures 2A–2B and 2F).

Having observed key differences in the accessibility landscape induced by CGRP and NMU, we next sought potential transcriptional regulators of these differences. We identified several families of transcription factors whose motifs were enriched in chromatin regions selectively opened by NMU (bZIP, NFkB(RHD), Zinc finger, NFAT) versus CGRP (ETS, GATA, RUNX) (Figure 4D). This analysis of neuropeptide-dependent modulation of chromatin accessibility identified distinct tran-

scription factors that likely underlie both the differential (*Il13*) and coordinate (*Il5*) regulation of key regulated genes.

Signaling Downstream of CGRP Involves cAMP to Shape Unique Gene Expression Profile Manifested by IL-5

We next sought to clarify the modes of intracellular signaling downstream of CGRP and NMU in ILC2s. IL-33 induces activation of NF- κ B, p38, and Erk, and NMU further promotes NFAT activation (Cardoso et al., 2017; Furusawa et al., 2013; Nagashima et al., 2018). We also observed that an NF- κ B inhibitor completely abrogated cytokine production induced by IL-33 and neuropeptides (Figure S4A). A p38 inhibitor strongly suppressed the actions of IL-33 with or without NMU on cytokines but had no effect on CGRP regulation of IL-5. Furthermore, CGRP had no effect on the nuclear translocation of NF- κ B (p65) and NFAT1 transcription factors induced by IL-33 and NMU, indicating that CGRP-mediated repression was not mediated by interfering with these transcription factors (Figures S4B and S4C).

cAMP, a known CGRP second messenger in other cells (Russell et al., 2014), was highly induced in ILC2s by CGRP but not by IL-33 and NMU (Figure 5A). To assess whether production of cAMP was sufficient to explain CGRP's actions in ILC2s, we used a cell-membrane-permeable cAMP analog. We found that dibutyryl-cAMP recapitulated the effects of CGRP on cell proliferation and discordant regulation of IL-5 and IL-13 production induced by IL-33. (Figures 5B–5D). One known downstream mediator of cAMP action is the transcription factor cAMP response element binding protein (CREB) (Russell et al., 2014). We observed that CREB phosphorylation was induced by CGRP and dibutyryl-cAMP but also by IL-33 and NMU (Figure 5E).

To evaluate the role for G α q and CREB downstream of NMU and CGRP receptor, we next treated cells with inhibitors for these molecules. As anticipated, a G α q inhibitor efficiently abrogated NMU- but not CGRP-dependent IL-5 and IL-13 production (Figures S4D and S4E). We also observed that a CREB inhibitor strongly suppressed CGRP induction of IL-5 and a modest effect on IL-33 and IL-33+NMU-mediated induction. These data suggest that the CGRP-cAMP axis enhanced IL-5 production by activating CREB, which may be a shared component downstream of IL-33 and NMU that induces IL-5 expression (Figures S4D and S4E). However, NMU also acts through G α q to activate NFAT, which in turn acts on the *Il5*, *Il13*, and other relevant loci (Cardoso et al., 2017; Klose et al., 2017). Thus, consistent with ligand-induced chromatin landscape alterations, it appears

(B) Pooled data showing percentage of IL-13-positive (left) or IL-5-positive (right) ILC2s cultured with indicated neuropeptide and/or cytokine as in (A).

(C) Principal-component (PC) analysis of gene expression using bulk mRNA-seq of lung ILC2s cultured under the indicated seven conditions for 4 h. Two replicates were analyzed per condition.

(D) Heatmap depicting 958 differentially expressed genes (DEG) (>3 log2-fold change and >10 FPKM expression in at least one sample) in samples shown in (C). Four groups of genes were defined using hierarchical clustering.

(E) Comparison of gene expression in ILC2s stimulated with IL-33+NMU versus IL-33+CGRP. Representative DEGs are depicted.

(F) Expression of selected cytokine genes across various conditions.

(G) Isolated ILC2s (5×10^3) were cultured under the indicated culture conditions for 5 days, and cell counts were recorded.

(H and I) The concentration of the indicated cytokines in the supernatant from cultures as in (G), assessed by Legendplex (H) or ELISA (I).

(J) Transcript expression of *Calca* and receptors for neuropeptides across conditions, quantitated by mRNA-seq (dataset shown in C and D).

Statistical significance are depicted as * $p < 0.05$, ** $p < 0.01$, and *** $p < 0.001$ (Student's t test). Data are from two (C and D) or average (E, F, and J) from two independent experiments or representative (A, G, H, I) or pool (B) from three independent experiments with similar results. (Average \pm SD from three experiments [B] or triplicated samples [G, H, and I]). See also Figure S3 and Table S2.

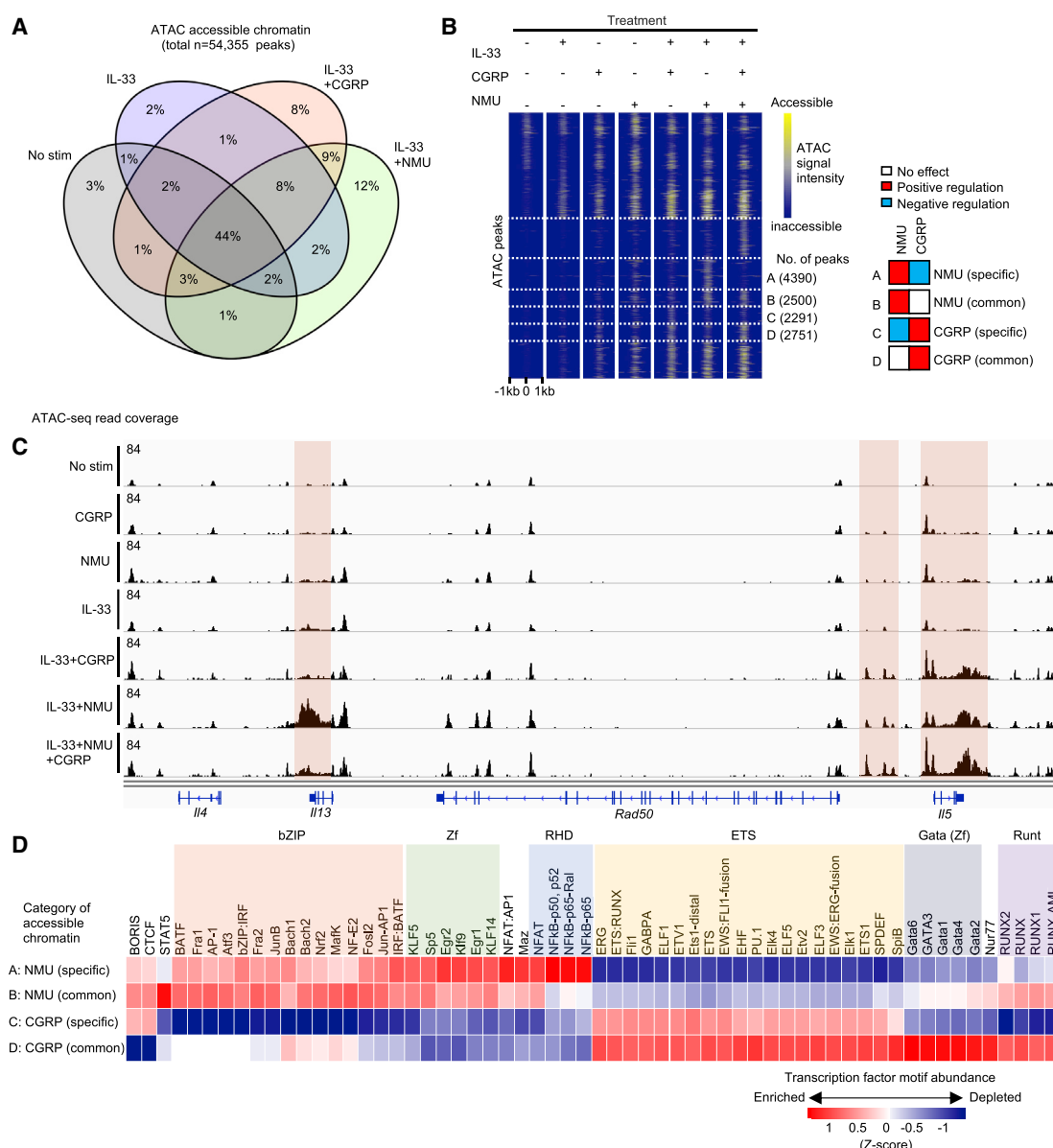


Figure 4. Differential Effects of CGRP and NMU on ILC2 Regulatory Elements

(A) Venn diagram demonstrating percentages of 54,355 chromatin-accessible regions identified by FastATAC-seq among ILC2s treated with or without IL-33, CGRP, and NMU for 4 h.

(B) Heatmap illustrating the chromatin accessibility among the dynamic regions shown in (A), highlighting four categories of differentially accessible regions. Categories A and B represent NMU-targeted regions that are antagonized by (A) or independent of (B) CGRP. Categories C and D represent CGRP-targeted regions that are counteracted by (C) or independent of (D) NMU.

(C) Genomic track view of Th2 cytokine loci showing distinct regulation of chromatin accessibility of *Il5* and *Il13* loci across different conditions.

(D) Heatmap showing relative enrichment of transcription factor motifs within chromatin regions categorized in (B).

Data are from representative of two independent experiments with similar results (C).

that distinct pathways converge to positively regulate the *Il5* locus.

To elucidate the global effects of cAMP and G α q pathways downstream of CGRP and NMU, we compared the effect of neuropeptides on ILC2 transcriptome with cAMP or a G α q inhibitor. We found that the dibutyryl-cAMP transcriptome and the CGRP transcriptome were relatively similar based on the Pearson correlation calculation (0.974) (Figure 5F). Similarly,

the transcriptomic comparison between IL-33 alone and IL33+NMU+G α q inhibitor was nearly identical (0.997), suggesting that most of NMU's effects were completely abrogated by the G α q inhibitor (Figure 5F).

To gain further insight underlying the biological processes distinctively regulated by CGRP and NMU, we performed pathway analysis on the modules selectively induced by these factors (Figure S5A). The enriched biological processes as well

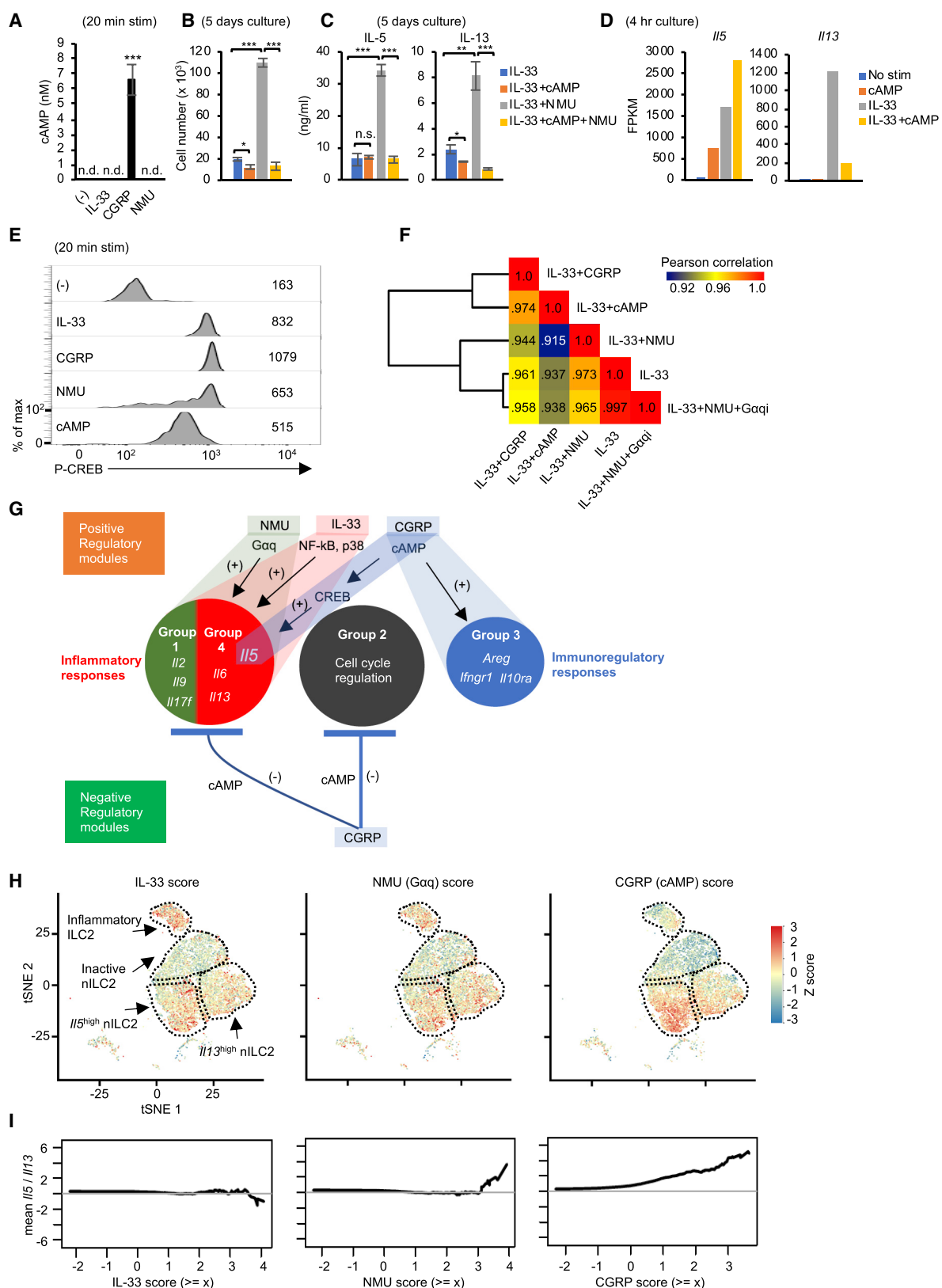


Figure 5. Signaling Downstream of CGRP Is Mediated by cAMP to Shape Unique ILC2 Gene Expression Profiles, Including In Vivo IL-5 Expression
 (A) cAMP concentration in the cell lysates of lung ILC2s without stimulation (-) or stimulated with IL-33, CGRP or NMU (20 min) as assessed by ELISA.
 (B) Isolated ILC2 (5×10^3) were cultured under the indicated conditions for 5 days, after which cell counts were recorded.

(legend continued on next page)
Immunity 51, 1–14, September 17, 2019 9

as representative genes associated with each module included: inflammatory (IL-17) response (group 1: *Il17f*), cell-cycle regulation (group 2: *Ccnd*, *Cdkn*), immunoregulatory response (group 3: *Areg*, *Ifngr1*, *Il10ra*) and inflammatory (Th2) response (group 4: *Il5*, *Il13*, *Il6*) (Figures 3D and S5A). CREB was predicted to be the main regulator of the group 3 genes (Figure S5B). On the other hand, NF- κ B and NFATC2 were enriched in the group 4 module cooperatively activated by NMU and IL-33 and constrained by CGRP. These effects are consistent with the view that CGRP acts predominantly via G α s and cAMP whereas NMU acts via G α q (Klose et al., 2017; Russell et al., 2014).

Having defined the transcriptional modules regulated by NMU and CGRP that act through distinct signaling pathways (Figures 3 and 5), we sought to use this *in vitro* information to interrogate the *in vivo* dynamics of ILC2 responses as measured by scRNA-seq following helminth infection. Specifically, we scored each GATA3-expressing ILC based on its expression of the IL-33, NMU (G α q), and CGRP (cAMP) modules (Table S3) and used these scores as proxies for signals sensed by cells (Figure S5C). The IL-33 and NMU (G α q) modules both developed and peaked at day 5 following infection. In contrast, the CGRP (cAMP) module rapidly developed and peaked at day 2 (Figure S5C).

Next, we evaluated phenotypic heterogeneity across the ILC2 single-cell clusters by visualizing their expression of the IL-33, NMU, and CGRP signature modules (Figure 5H). Both IL-33 (left) and NMU (G α q) (middle) signatures were distributed across active ILC2 subsets, though both were modestly enriched in inflammatory ILC2. In contrast, the CGRP signature (which approximated a cAMP signature) (right) was highly enriched in the *Il5^{hi}* ILC2 subset, suggesting that CGRP was most relevant in modulating this subset following helminth infection.

Having demonstrated the divergent regulation of IL-13 and IL-5 by CGRP versus NMU or IL-33 *in vitro* (Figure 3 and 4), we next examined the balance of IL-5 and IL-13 expression in ILC2s *in vivo* upon infection. Cells receiving IL-33 (Figure 5I, left) or NMU (Figure 5I, middle) signals maintained equivalent expression of *Il5* and *Il13* (shown in y axis). In contrast, cells receiving a stronger CGRP signal exhibited higher *Il5* expression (Figure 5I, right). These results were in line with the kinetics of *Il5* and *Il13* expression as detected by single-cell and bulk mRNA-seq (Figures 1F and 1G). Collectively, our data argue for a dynamic role of the CGRP-cAMP axis in ILC2 responses following helminth infection and, in particular, the selective modulation of IL-5 and IL-13 and tuning type 2 immune responses during infectious challenge.

CGRP Suppresses IL-33-Mediated Pulmonary Inflammation and Worm Expulsion of *N. brasiliensis*

We next explored whether our *in vitro* observations were relevant to pulmonary host defense *in vivo*. To test this, we challenged *Rag1^{-/-}* or *Rag2^{-/-}* mice with intranasal administration of IL-33 to activate ILC2s and induce lung inflammation (Figure 6A). As expected, IL-33 induced severe lung pathology as evidenced by enhanced cell infiltration and goblet cell hyperplasia (Figures 6B and 6C) as well as increased numbers of eosinophils and ILC2s in the lung and bronchoalveolar lavage fluid (BALF). We found that CGRP significantly reduced IL-33-mediated inflammation as measured by all these parameters (Figures 6D–6F).

Next, we challenged wild-type and *Calca^{gfp/gfp}* mice (which lack transcripts of both of calcitonin and α -CGRP) with IL-33 to assess the role of endogenous CGRP to control IL-33-induced lung inflammation (Figures S6A–S6C). Although *Calca^{gfp/gfp}* mice had comparable numbers of eosinophils, ILC2s, and Th cells at the steady state (Figure S6A), *Calca^{gfp/gfp}* mice showed higher accumulation of ILC2s and Th cells in BALF following IL-33 intranasal administration (Figures S6B and S6C). Although there was a trend toward increased accumulation of eosinophils in *Calca^{gfp/gfp}* mice, the difference with wild-type mice did not attain significance ($p = 0.07$) (Figures S6B and S6C). Collectively, these data indicated that CGRP is required to constrain IL-33-mediated ILC2 responses and subsequent inflammatory cell infiltration *in vivo*.

Next, we challenged wild-type and α -CGRP-deficient (α -CGRP^{-/-}) mice with *N. brasiliensis* to evaluate the role of endogenous CGRP to control helminth infection (Figure 6G). α -CGRP^{-/-} mice showed enhanced intestinal worm expulsion with increased numbers of ILC2s in mesenteric lymph nodes (mLN) (Figures 6H and 6I). The results indicate that in response to helminth infection, endogenous production of CGRP is a negative regulator of ILC2 responses, consistent with our *in vitro* observations and also with our *in vivo* IL-33-induced lung inflammation.

Having observed that endogenous tissue CGRP acts to constrain ILC2 activation induced by helminth infection, we next asked whether genetic interference with CGRP signaling within hematopoietic cell compartments affects type 2 immune response. To this end, we used mice in which Ramp1, a component of CGRP receptor complex, was deleted. Irradiated *Rag2^{-/-}* *gc^{-/-}* mice were reconstituted with bone marrow from wild-type or *Ramp1^{-/-}* mice to specifically eliminate CGRP sensing on hematopoietic cells in the host. The reconstituted hosts were then

(C) Concentration of cytokines in the supernatant from cultures depicted in (B), assessed by Legendplex.

(D) Expression of *Il5* and *Il13* in lung ILC2s cultured under the indicated conditions, confirmed by bulk mRNA-seq. Two replicates were analyzed per condition.

(E) Phospho-CREB (Ser133) was measured by flow cytometric analysis of lung ILC2s following the indicated stimulations for 20 min.

(F) Global transcriptomic similarities between the indicated conditions were evaluated by Pearson correlations calculated based on log2 (FPKM + 1) from the average of replicates. Gene expression data for IL-33, IL-33+CGRP, IL-33+NMU, or IL-33+cAMP conditions are from data depicted in (D) and Figure 3C. G α q, G α q inhibitor

(G) Inferred transcriptional modules in ILC2s regulated by IL-33 and neuropeptides. See also Figures S5A and S5B.

(H) Single-cell scores of representative transcriptional modules (IL-33, NMU, CGRP) in ILC2s from mice with *N. brasiliensis* infection as in Figure 1A. The gene modules were generated using bulk RNA-seq data from ILC2s treated with IL-33, NMU, or CGRP compared to unstimulated cells. IL-33, NMU, and CGRP module scores were projected onto separate tSNE representations of ILCs (from Figure 1C). Scores are comparable within a module across time points but not across modules.

(I) The ratio of *Il5* to *Il13* abundance (log-space) in all cells is shown as a function of module score thresholds.

Statistical significance are depicted as * $p < 0.05$, ** $p < 0.01$, and *** $p < 0.001$ (Student's *t* test). Data are representative from three independent experiments (A–C) or representative from two independent experiments with similar results (E). (Average \pm SD from triplicated well in A–C). See also Figures S4 and S5 and Table S3.

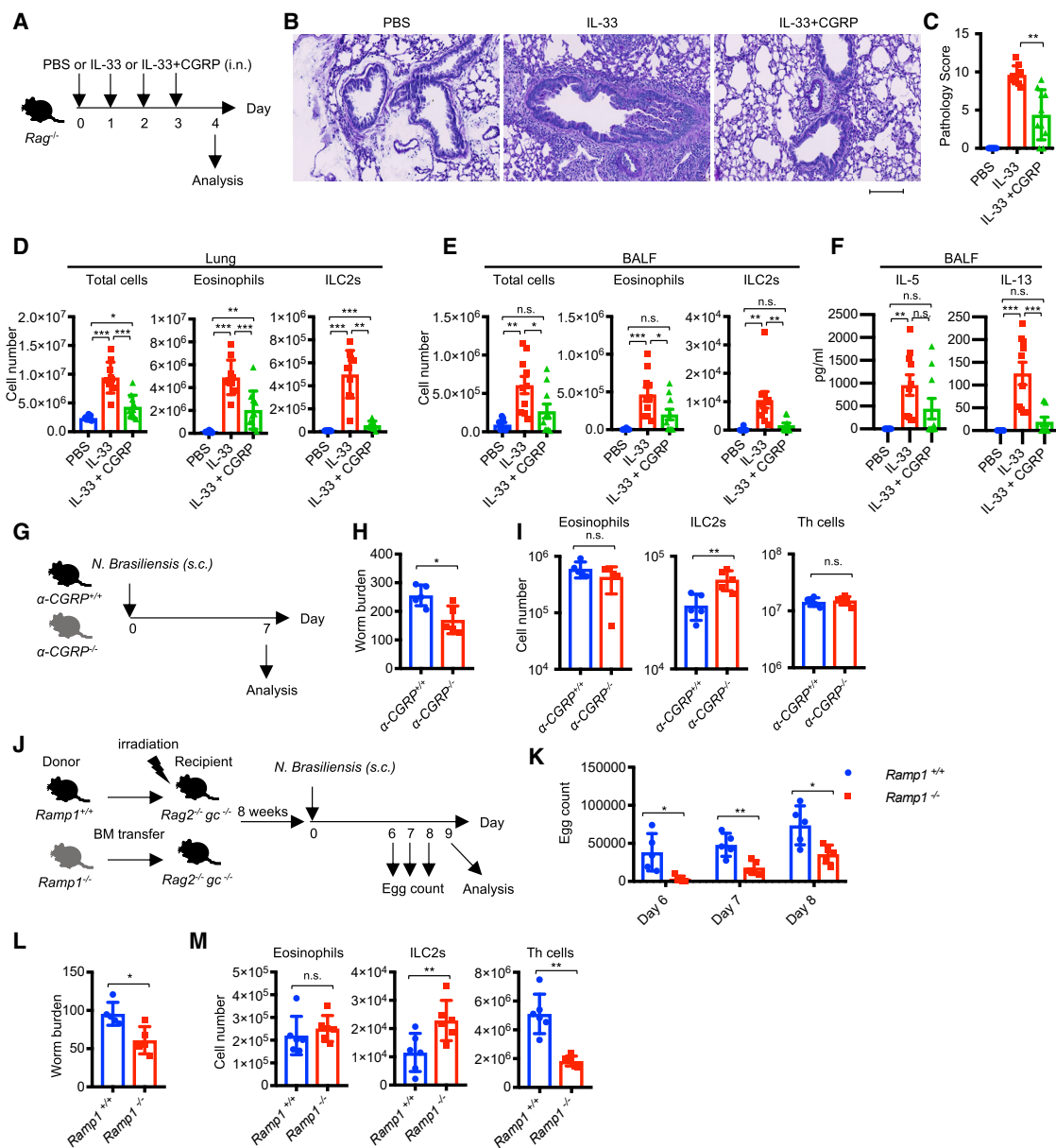


Figure 6. CGRP Is Required for Negatively Regulating ILC2s and Type 2 Responses In Vivo

(A–F) Effect of CGRP in IL-33-induced pulmonary inflammation. (A) *Rag1^{-/-}* or *Rag2^{-/-}* mice were administered PBS (n = 8), IL-33 (n = 10), or IL-33+CGRP (n = 10) intranasally for 4 consecutive days, with the following analyses of lung pathology 1 day after the last administration: (B) periodic acid-Schiff (PAS) staining, (C) pathology score, (D) cell count of total cells, eosinophils (CD11c⁻ CD11b⁺ Siglec-F⁺) and ILC2s (Lin⁻ Thy1⁺ CD127⁺ GATA3⁺), and (E and F) cell counts (E) and cytokine production (F) in BALF. (B) Scale bar, 100 μ m.

(G–I) Impact of genetic deletion of CGRP on helminth infection: experimental scheme (G) and worm count of small intestine (H) or cell numbers of eosinophils, ILC2s, and Th cells (I) in mLNs from *α-CGRP^{+/+}* (n = 5) or *α-CGRP^{-/-}* (n = 5) mice infected with *N. brasiliensis* and analyzed at day 7 post infection.

(J–M) Impact of genetic deletion of CGRP receptor subunit Ramp1 in transferred hematopoietic cells following helminth infection: experimental scheme (J). Fecal egg counts (K), small intestine worm counts (L), numbers of eosinophils, ILC2s, and Th cells (M) in lungs were assessed in irradiated chimeric *Rag2^{-/-} gc^{-/-}* mice reconstituted with the bone marrow from either wild-type (n = 5) or *Ramp1^{-/-}* (n = 5) mice infected with *N. brasiliensis* on day 9 post infection.

Each symbol represents an individual mouse (C–F, H and I, K–M). Statistical significance is depicted as *p < 0.05, **p < 0.01, and ***p < 0.001 (Student's t test). Data are from representative (B, H, I) or pool (C–F) of two experiments with similar results or from one experiment (K–M). See also Figure S6.

challenged with helminth infection (Figure 6J). In mice reconstituted with *Ramp1^{-/-}* bone marrow, we observed reduced numbers of eggs in the feces as well as reduced worm burden in the small intestine along with enhanced ILC2 responses but

reduced Th2 cell response following *N. brasiliensis* infection (Figures 6K–6M). Collectively, our results demonstrate that sensing of environmental CGRP signals by ILC2s leads to limited magnitude of their responses to infection *in vivo*.

DISCUSSION

In this study, we used single-cell transcriptomic analysis and identified heterogeneous populations of ILC2s, preferentially expressing either *Il5* (*Il5^{hi}* ILC2s) or *Il13* (*Il13^{hi}* ILC2s); both populations emerged during helminth infection but with distinct kinetics. We also identified a neuropeptide, CGRP, which antagonized many actions of the neuropeptide NMU and the alarmin IL-33 but promoted IL-5 production. Accordingly, CGRP suppressed type 2 immune responses mediated by IL-33 or helminth infection, suggesting context-dependent immunoregulatory effect of CGRP on ILC2 responses *in vivo*.

The neuroimmune interactions at peripheral barrier tissues are increasingly appreciated clinically and experimentally (Klose and Artis, 2019; Pavlov and Tracey, 2017; Veiga-Fernandes and Mucida, 2016) and led to the term “neuroimmune cell units” (NICUs) to denote their functional interaction (Veiga-Fernandes and Pachnis, 2017). Interest in neuronal-lymphocyte crosstalk has been augmented by recent reports that neuropeptides directly impact tissue-resident mucosal innate immune cells. (Veiga-Fernandes and Artis, 2018). Specifically, cholinergic neurons adjacent to intestinal and pulmonary ILC2s produce the neuropeptide NMU, which acts via NMUR1 selectively expressed by ILC2s to induce the production of type 2 cytokines (Cardoso et al., 2017; Klose et al., 2017; Wallrapp et al., 2017). Sympathetic neurons also innervate these areas, and their product, β adrenergic agonists counteracts the action of IL-33 and dampen ILC2 responses (Moriyama et al., 2018).

The data presented herein help to resolve some of the apparent contradictory effects of CGRP in the lung. CGRP induces very distinct ILC2 transcriptomic and epigenomic programs compared to NMU in the presence or absence of the alarmin IL-33, with the dominant outcome being opposition of IL-33 and NMU effects. Specifically, CGRP inhibited the production of many proinflammatory cytokines produced by ILC2s. In part, the negative regulatory effect of CGRP on ILC2s can be explained by its inhibitory effect on cell growth, an effect of CGRP that has been noted for more than 25 years (Boudard and Bastide, 1991; Umeda et al., 1988). CGRP has been shown to exert its effect through G α s to induce production of cAMP, and we confirmed that this was the case in ILC2s. Therefore, the effect of CGRP on ILC2s is consistent with the general view that cAMP production limits lymphocyte proliferation. Globally, our data showed that exposing ILC2s to a cell-permeant form of cAMP mimicked many of the transcriptomic effects of CGRP. By contrast, NMU exerts its effect via G α q. Accordingly, administration of CGRP limited IL-33-induced pulmonary immunopathology, while CGRP-deficient mice showed severe symptoms and pathology. In addition, CGRP-deficient mice exhibited enhanced intestinal worm expulsion following helminth infection along with enhanced ILC2 expansion. This outcome on ILC2s was phenocopied by hematopoietic reconstitution of immunodeficient mice with *Ramp1*^{-/-} bone marrow, which eliminated CGRP signaling in ILC2 and other blood cells. Taken together, the observed repressive effects of CGRP on ILC2 responses are consistent with the view that CGRP suppresses lymphocyte

proliferation through cAMP generation. It is of note that we observed discordant effects of *Ramp1* deletion on T cells and ILC2 regarding cell numbers. Additional studies using cell-type-specific deletion of CGRP or its cognate receptors will be needed to further decipher the relative importance of the CGRP-cAMP axis in different cell types *in vivo*.

While predominantly suppressive effect of CGRP on ILC2s is evident, the promotion of IL-5 production is a notable exception that exemplifies the proinflammatory action of CGRP. Although type 2 responses collectively refer to the production of the cytokines IL-4, IL-5, and IL-13, whose genes are clustered together on the same chromosome, these cytokines can be discoordinateably regulated. For instance, IL-5-producing Th2 cells represent a highly differentiated or pathogenic subset (Nakayama et al., 2017; Upadhyaya et al., 2011). In fact, our single-cell data also show distinct subsets of activated ILC2s separable as *Il5^{hi}* ILC2 and *Il13^{hi}* ILC2, supporting the notion that distinct subsets of type 2 immune cells might reflect different pathogenic potential. It is also conceivable that the reason why eosinophilia was not affected by the lack of CGRP signaling in helminth infection may be attributable to CGRP’s complex effects on IL-5 and ILC2 homeostasis.

Another finding in our report is that in the setting of helminth infection, a relevant immune cell population (ILC2s) expresses *Calca*, which encodes CGRP. CGRP has been previously found in non-neuronal cells, such as endothelial cells and adipocytes, and there is some evidence that it is also produced by several immune cell types, including activated B lymphocytes, mitogen-activated peripheral blood mononuclear cells, and macrophages (Russell et al., 2014). Our mRNA-seq and ATAC-seq data (Shih et al., 2016) are notable in that ILC2s, but not other ILC subsets, express *Calca*. Thus, the accessibility of *Calca* locus is programmed at the ILC2 precursor stage, allowing ILC2s to rapidly produce this neuropeptide upon activation. Elucidating the significance of lymphoid-derived versus neural-derived CGRP will be important.

Corresponding to its role as a potent vasodilator, CGRP and its receptor have been clinically targeted by a variety of monoclonal antibodies, which are efficacious in the prevention and treatment of migraine (Mitsikostas and Reuter, 2017; Walter and Bigal, 2015). The reported side effects of CGRP blockade include infection, consistent with findings of Baral et al. (2018). However, given the complexity of the effects of CGRP and NMU, much is still to be learned about the consequences of blocking these neuropeptides to various immune responses and disorders characterized by dysregulated inflammatory cytokines. The action of CGRP to tilt the balance between IL-5 and IL-13 will become quite consequential in situations such as pulmonary arterial hypertension in which IL-5-producing ILC2 and eosinophils play pivotal roles (Ikutani et al., 2017) or tissue fibrosis in which IL-13 is an important driver (Gieseck et al., 2018). Understanding the contribution of ILCs, their effector cytokines, and the role of CGRP in tissue damage and repair is clearly an important area for future research. The current clinical use of CGRP antagonists, both monoclonal antibodies and small molecules, indicates that advances in understanding the role of CGRP in lung immunopathology and other settings will be rapidly translated.

STAR METHODS

Detailed methods are provided in the online version of this paper and include the following:

- KEY RESOURCES TABLE
- LEAD CONTACT AND MATERIALS AVAILABILITY
- EXPERIMENTAL MODEL AND SUBJECT DETAILS
- METHOD DETAILS
 - Mice
 - Preparation of cell suspensions from tissues
 - Flow cytometry
 - *In vitro* ILC2 culture
 - *Nippostrongylus brasiliensis* infection
 - IL-33-mediated pulmonary inflammation *in vivo*
 - Single-cell RNA sequencing (scRNA-seq)
 - Bulk mRNA sequencing
 - FastATAC sequencing
 - Imagestream
 - Measurement of cytokines and cAMP
 - Histological analysis
 - Immunofluorescence microscopy
- QUANTIFICATION AND STATISTICAL ANALYSIS
 - Bulk mRNA-seq analysis
 - ATAC-seq analysis
 - scRNA-seq analysis
 - Analyzing transcriptional modules
 - Statistical analysis
- DATA AND CODE AVAILABILITY

SUPPLEMENTAL INFORMATION

Supplemental Information can be found online at <https://doi.org/10.1016/j.immuni.2019.06.009>.

ACKNOWLEDGMENTS

We thank members of Molecular Immunology and Inflammation Branch (NIAMS) for input and support. We thank S. Dell'Orso, G. Gutierrez-Cruz, and F. Naz (Genome Analysis Core Facility, NIAMS); J. Simone, J. Lay, and K. Tinsley (Flow Cytometry Section, NIAMS); H-W. Sun and S.R. Brooks (Biodata Mining and Discovery Section, NIAMS); E. Ralston and A. Kenea (Light Imaging Section, NIAMS); and L. Samsel and P. J. McCoy (Flow Cytometry Core, NHLBI) for their technical support. This study utilized the high-performance computational capabilities of the Biowulf Linux cluster at the NIH. This work was supported by the Intramural Research Programs of NIAMS and NIAID. Research in the Artis laboratory is supported by the National Institutes of Health (AI074878, AI095466, AI095608, and AI102942), the Burroughs Wellcome Fund, the Crohn's & Colitis Foundation, Cure for IBD, and the Rosanne H. Silberman Foundation. H.N. was supported by the JSPS Research Fellowship for Japanese Biomedical and Behavioral Researchers at NIH. T.M. was supported by the Crohn's & Colitis Foundation.

AUTHOR CONTRIBUTIONS

H.N. and T.M. designed the project and performed and analyzed experiments with assistance and advice from H.-Y.S., F.P.D., F.M., Y.H., O.J.H., C.Y., and Y.M. H.-Y.S. performed and analyzed ATAC-seq. F.P.D. performed computational analysis. J.F.U. and K.M.C. contributed to analytical tools and input regarding experimental design. K.M.C., Y.B., D.A., Y.K., and J.J.O. planned and supervised this project. H.N., T.M., D.A., Y.K. and J.J.O. wrote the manuscript with input, advice, and revisions from all authors.

DECLARATION OF INTERESTS

D.A. has contributed to scientific advisory boards at MedImmune, Pfizer, FARE, and the KRF.

Received: April 22, 2019

Revised: June 12, 2019

Accepted: June 14, 2019

Published: July 25, 2019

REFERENCES

- Artis, D., and Spits, H. (2015). The biology of innate lymphoid cells. *Nature* **517**, 293–301.
- Baral, P., Umans, B.D., Li, L., Wallrapp, A., Bist, M., Kirschbaum, T., Wei, Y., Zhou, Y., Kuchroo, V.K., Burkett, P.R., et al. (2018). Nociceptor sensory neurons suppress neutrophil and $\gamma\delta$ T cell responses in bacterial lung infections and lethal pneumonia. *Nat. Med.* **24**, 417–426.
- Bentley, D.R., Balasubramanian, S., Swerdlow, H.P., Smith, G.P., Milton, J., Brown, C.G., Hall, K.P., Evers, D.J., Barnes, C.L., Bignell, H.R., et al. (2008). Accurate whole human genome sequencing using reversible terminator chemistry. *Nature* **456**, 53–59.
- Boudard, F., and Bastide, M. (1991). Inhibition of mouse T-cell proliferation by CGRP and VIP: effects of these neuropeptides on IL-2 production and cAMP synthesis. *J. Neurosci. Res.* **29**, 29–41.
- Bray, N.L., Pimentel, H., Melsted, P., and Pachter, L. (2016). Near-optimal probabilistic RNA-seq quantification. *Nat. Biotechnol.* **34**, 525–527.
- Cardoso, V., Chesné, J., Ribeiro, H., García-Cassani, B., Carvalho, T., Bouchery, T., Shah, K., Barbosa-Morais, N.L., Harris, N., and Veiga-Fernandes, H. (2017). Neuronal regulation of type 2 innate lymphoid cells via neuromedin U. *Nature* **549**, 277–281.
- Corces, M.R., Buenrostro, J.D., Wu, B., Greenside, P.G., Chan, S.M., Koenig, J.L., Snyder, M.P., Pritchard, J.K., Kundaje, A., Greenleaf, W.J., et al. (2016). Lineage-specific and single-cell chromatin accessibility charts human hematopoiesis and leukemia evolution. *Nat. Genet.* **48**, 1193–1203.
- Diefenbach, A., Colonna, M., and Koyasu, S. (2014). Development, differentiation, and diversity of innate lymphoid cells. *Immunity* **41**, 354–365.
- Eberl, G., Colonna, M., Di Santo, J.P., and McKenzie, A.N. (2015). Innate lymphoid cells. Innate lymphoid cells: a new paradigm in immunology. *Science* **348**, aaa6566.
- Furusawa, J., Moro, K., Motomura, Y., Okamoto, K., Zhu, J., Takayanagi, H., Kubo, M., and Koyasu, S. (2013). Critical role of p38 and GATA3 in natural helper cell function. *J. Immunol.* **191**, 1818–1826.
- Gieseck, R.L., 3rd, Wilson, M.S., and Wynn, T.A. (2018). Type 2 immunity in tissue repair and fibrosis. *Nat. Rev. Immunol.* **18**, 62–76.
- Heinz, S., Benner, C., Spann, N., Bertolino, E., Lin, Y.C., Laslo, P., Cheng, J.X., Murre, C., Singh, H., and Glass, C.K. (2010). Simple combinations of lineage-determining transcription factors prime cis-regulatory elements required for macrophage and B cell identities. *Mol. Cell* **38**, 576–589.
- Holzmann, B. (2013). Modulation of immune responses by the neuropeptide CGRP. *Amino Acids* **45**, 1–7.
- Huang, Y., Guo, L., Qiu, J., Chen, X., Hu-Li, J., Siebenlist, U., Williamson, P.R., Urban, J.F., Jr., and Paul, W.E. (2015). IL-25-responsive, lineage-negative KLRG1(hi) cells are multipotential 'inflammatory' type 2 innate lymphoid cells. *Nat. Immunol.* **16**, 161–169.
- Ikutani, M., Tsuneyama, K., Kawaguchi, M., Fukuoka, J., Kudo, F., Nakae, S., Arita, M., Nagai, Y., Takaki, S., and Takatsu, K. (2017). Prolonged activation of IL-5-producing ILC2 causes pulmonary arterial hypertrophy. *JCI Insight* **2**, e90721.
- Klose, C.S., and Artis, D. (2019). Neuronal regulation of innate lymphoid cells. *Curr. Opin. Immunol.* **56**, 94–99.
- Klose, C.S.N., Mahlaköivi, T., Moeller, J.B., Rankin, L.C., Flamar, A.L., Kabata, H., Monticelli, L.A., Moriyama, S., Putzel, G.G., Rakhilin, N., et al. (2017). The neuropeptide neuromedin U stimulates innate lymphoid cells and type 2 inflammation. *Nature* **549**, 282–286.

- Langmead, B., Trapnell, C., Pop, M., and Salzberg, S.L. (2009). Ultrafast and memory-efficient alignment of short DNA sequences to the human genome. *Genome Biol.* 10, R25.
- Li, M., Wetzel-Strong, S.E., Hua, X., Tilley, S.L., Oswald, E., Krummel, M.F., and Caron, K.M. (2014). Deficiency of RAMP1 attenuates antigen-induced airway hyperresponsiveness in mice. *PLoS ONE* 9, e102356.
- Lu, J.T., Son, Y.J., Lee, J., Jetton, T.L., Shioya, M., Moscoso, L., Niswender, K.D., Loewy, A.D., Magnuson, M.A., Sanes, J.R., and Emeson, R.B. (1999). Mice lacking alpha-calcitonin gene-related peptide exhibit normal cardiovascular regulation and neuromuscular development. *Mol. Cell. Neurosci.* 14, 99–120.
- Macosko, E.Z., Basu, A., Satija, R., Nemesh, J., Shekhar, K., Goldman, M., Tirosh, I., Bialas, A.R., Kamitaki, N., Martersteck, E.M., et al. (2015). Highly Parallel Genome-wide Expression Profiling of Individual Cells Using Nanoliter Droplets. *Cell* 161, 1202–1214.
- Mitsikostas, D.D., and Reuter, U. (2017). Calcitonin gene-related peptide monoclonal antibodies for migraine prevention: comparisons across randomized controlled studies. *Curr. Opin. Neurol.* 30, 272–280.
- Morita, H., Moro, K., and Koyasu, S. (2016). Innate lymphoid cells in allergic and nonallergic inflammation. *J. Allergy Clin. Immunol.* 138, 1253–1264.
- Moriyama, S., Brestoff, J.R., Flamar, A.L., Moeller, J.B., Klose, C.S.N., Rankin, L.C., Yudanin, N.A., Monticelli, L.A., Putzel, G.G., Rodewald, H.R., and Artis, D. (2018). β_2 -adrenergic receptor-mediated negative regulation of group 2 innate lymphoid cell responses. *Science* 359, 1056–1061.
- Moro, K., Yamada, T., Tanabe, M., Takeuchi, T., Ikawa, T., Kawamoto, H., Furusawa, J., Ohtani, M., Fujii, H., and Koyasu, S. (2010). Innate production of T(H)2 cytokines by adipose tissue-associated c-Kit(+)Sca-1(+) lymphoid cells. *Nature* 463, 540–544.
- Nagashima, H., Okuyama, Y., Fujita, T., Takeda, T., Motomura, Y., Moro, K., Hidaka, T., Omori, K., Sakurai, T., Machiyama, T., et al. (2018). GITR cosignal in ILC2s controls allergic lung inflammation. *J. Allergy Clin. Immunol.* 141, 1939–1943.e8.
- Nakayama, T., Hirahara, K., Onodera, A., Endo, Y., Hosokawa, H., Shinoda, K., Tumes, D.J., and Okamoto, Y. (2017). Th2 Cells in Health and Disease. *Annu. Rev. Immunol.* 35, 53–84.
- Pavlov, V.A., and Tracey, K.J. (2017). Neural regulation of immunity: molecular mechanisms and clinical translation. *Nat. Neurosci.* 20, 156–166.
- Pimentel, H., Bray, N.L., Puente, S., Melsted, P., and Pachter, L. (2017). Differential analysis of RNA-seq incorporating quantification uncertainty. *Nat. Methods* 14, 687–690.
- Quinlan, A.R., and Hall, I.M. (2010). BEDTools: a flexible suite of utilities for comparing genomic features. *Bioinformatics* 26, 841–842.
- R Development Core Team (2018). R: A language and environment for statistical computing (R Foundation for Statistical Computing).
- Rankin, L.C., and Artis, D. (2018). Beyond Host Defense: Emerging Functions of the Immune System in Regulating Complex Tissue Physiology. *Cell* 173, 554–567.
- Ricardo-Gonzalez, R.R., Van Dyken, S.J., Schneider, C., Lee, J., Nussbaum, J.C., Liang, H.E., Vaka, D., Eckalbar, W.L., Molofsky, A.B., Erle, D.J., and Locksley, R.M. (2018). Tissue signals imprint ILC2 identity with anticipatory function. *Nat. Immunol.* 19, 1093–1099.
- Robinette, M.L., Fuchs, A., Cortez, V.S., Lee, J.S., Wang, Y., Durum, S.K., Gilfillan, S., and Colonna, M.; Immunological Genome Consortium (2015). Transcriptional programs define molecular characteristics of innate lymphoid cell classes and subsets. *Nat. Immunol.* 16, 306–317.
- Russell, F.A., King, R., Smillie, S.J., Kodji, X., and Brain, S.D. (2014). Calcitonin gene-related peptide: physiology and pathophysiology. *Physiol. Rev.* 94, 1099–1142.
- Shih, H.Y., Sciumè, G., Mikami, Y., Guo, L., Sun, H.W., Brooks, S.R., Urban, J.F., Jr., Davis, F.P., Kanno, Y., and O'Shea, J.J. (2016). Developmental Acquisition of Regulomes Underlies Innate Lymphoid Cell Functionality. *Cell* 165, 1120–1133.
- Shinoda, K., Hirahara, K., Iinuma, T., Ichikawa, T., Suzuki, A.S., Sugaya, K., Tumes, D.J., Yamamoto, H., Hara, T., Tani-Ichi, S., et al. (2016). Thy1+IL-7+ lymphatic endothelial cells in iBALT provide a survival niche for memory T-helper cells in allergic airway inflammation. *Proc. Natl. Acad. Sci. USA* 113, E2842–E2851.
- Sonnenberg, G.F., and Artis, D. (2015). Innate lymphoid cells in the initiation, regulation and resolution of inflammation. *Nat. Med.* 21, 698–708.
- Spits, H., and Cupedo, T. (2012). Innate lymphoid cells: emerging insights in development, lineage relationships, and function. *Annu. Rev. Immunol.* 30, 647–675.
- Sui, P., Wiesner, D.L., Xu, J., Zhang, Y., Lee, J., Van Dyken, S., Lashua, A., Yu, C., Klein, B.S., Locksley, R.M., et al. (2018). Pulmonary neuroendocrine cells amplify allergic asthma responses. *Science* 360, eaan8546.
- Thorvaldsdóttir, H., Robinson, J.T., and Mesirov, J.P. (2013). Integrative Genomics Viewer (IGV): high-performance genomics data visualization and exploration. *Brief Bioinform.* 14, 178–192.
- Trapnell, C., Roberts, A., Goff, L., Pertea, G., Kim, D., Kelley, D.R., Pimentel, H., Salzberg, S.L., Rinn, J.L., and Pachter, L. (2012). Differential gene and transcript expression analysis of RNA-seq experiments with TopHat and Cufflinks. *Nat. Protoc.* 7, 562–578.
- Umeda, Y., Takamiya, M., Yoshizaki, H., and Arisawa, M. (1988). Inhibition of mitogen-stimulated T lymphocyte proliferation by calcitonin gene-related peptide. *Biochem. Biophys. Res. Commun.* 154, 227–235.
- Upadhyaya, B., Yin, Y., Hill, B.J., Douek, D.C., and Prussin, C. (2011). Hierarchical IL-5 expression defines a subpopulation of highly differentiated human Th2 cells. *J. Immunol.* 187, 3111–3120.
- Veiga-Fernandes, H., and Artis, D. (2018). Neuronal-immune system cross-talk in homeostasis. *Science* 359, 1465–1466.
- Veiga-Fernandes, H., and Mucida, D. (2016). Neuro-Immune Interactions at Barrier Surfaces. *Cell* 165, 801–811.
- Veiga-Fernandes, H., and Pachnis, V. (2017). Neuroimmune regulation during intestinal development and homeostasis. *Nat. Immunol.* 18, 116–122.
- Wallrapp, A., Riesenfeld, S.J., Burkett, P.R., Abdulhour, R.E., Nyman, J., Dionne, D., Hofree, M., Cuoco, M.S., Rodman, C., Farouq, D., et al. (2017). The neuropeptide NMU amplifies ILC2-driven allergic lung inflammation. *Nature* 549, 351–356.
- Walter, S., and Bigal, M.E. (2015). TEV-48125: a review of a monoclonal CGRP antibody in development for the preventive treatment of migraine. *Curr. Pain Headache Rep.* 19, 6.
- Weinstein, J.N., Myers, T., Buolamwini, J., Raghavan, K., van Osdol, W., Licht, J., Viswanadhan, V.N., Kohn, K.W., Rubinstein, L.V., Koutsoukos, A.D., et al. (1994). Predictive statistics and artificial intelligence in the U.S. National Cancer Institute's Drug Discovery Program for Cancer and AIDS. *Stem Cells* 12, 13–22.
- Wilhelm, C., Hirota, K., Stieglitz, B., Van Snick, J., Tolaini, M., Lahli, K., Sparwasser, T., Helmby, H., and Stockinger, B. (2011). An IL-9 fate reporter demonstrates the induction of an innate IL-9 response in lung inflammation. *Nat. Immunol.* 12, 1071–1077.
- Xu, H., Luo, X., Qian, J., Pang, X., Song, J., Qian, G., Chen, J., and Chen, S. (2012). FastUniq: a fast de novo duplicates removal tool for paired short reads. *PLoS ONE* 7, e52249.
- Zhang, Y., Liu, T., Meyer, C.A., Eeckhoute, J., Johnson, D.S., Bernstein, B.E., Nusbaum, C., Myers, R.M., Brown, M., Li, W., and Liu, X.S. (2008). Model-based analysis of ChIP-Seq (MACS). *Genome Biol.* 9, R137.

STAR★METHODS

KEY RESOURCES TABLE

REAGENT or RESOURCE	SOURCE	IDENTIFIER
Antibodies		
Biotin-anti-mouse CD8a	Biolegend	RRID: AB_312743
Biotin-anti-mouse CD19	Biolegend	RRID: AB_313639
Biotin-anti-mouse CD11b	Biolegend	RRID: AB_312787
Biotin-anti-mouse CD11c	Biolegend	RRID: AB_313773
Biotin-anti-mouse TCR γ/δ	Biolegend	RRID: AB_313827
Biotin-anti-mouse Gr1	Biolegend	RRID: AB_313369
Biotin-anti-mouse CD49b	Biolegend	RRID: AB_313411
Biotin-anti-mouse TER-119	Biolegend	RRID: AB_313705
Biotin-anti-mouse Fc ϵ R1 α	Biolegend	RRID: AB_1626106
Biotin-anti-mouse CD38	Biolegend	RRID: AB_312669
PerCP/Cy5.5-anti-mouse CD11b	Biolegend	RRID: AB_893233
APC-anti-mouse CD11c	Biolegend	RRID: AB_313778
PE-anti-mouse TCR β	Biolegend	RRID: AB_313431
PE/Cy7-anti-mouse KLRG1	Biolegend	RRID: AB_2561736
APC-anti-mouse IL-5	Biolegend	RRID: AB_315330
PerCP/Cy5.5-anti-mouse CD4	Biolegend	RRID: AB_893326
PerCP/Cy5.5-anti-mouse CD3 ε (145-2C11)	Invitrogen	RRID: AB_1107000
PerCP/Cy5.5-anti-mouse CD5 (53-7.3)	Invitrogen	RRID: AB_914334
PerCP-eFluor 710-anti-mouse Fc ϵ RI (CRA1)	Invitrogen	RRID: AB_2573801
APC-Cy7-anti-mouse B220 (RA3-6B2)	Invitrogen	RRID: AB_529535
APC-Cy7-anti-mouse CD11b (M1/70)	Invitrogen	RRID: AB_1603193
APC-Cy7-anti-mouse CD11c (N418)	Invitrogen	RRID: AB_1548652
PerCP/Cy5.5-anti-mouse NK1.1 (PK136)	Invitrogen	RRID: AB_914361
FITC-anti-mouse KLRG1 (2F1)	Invitrogen	RRID: AB_1311265
BV650-anti-mouse CD45 (30-F11)	Biolegend	RRID: AB_2565884
PE/Cy7-anti-mouse CD127 (A7R34)	Biolegend	RRID: AB_1937265
PE-anti-mouse SiglecF (E50-2440)	BD Bioscience	RRID: AB_394341
AF700-anti-mouse CD90.2 (53-2.1)	Biolegend	RRID: AB_493725
BV421-anti-mouse ST2 (DIH9)	Biolegend	RRID: AB_2565634
BUV395-anti-mouse CD4 (GK1.5)	BD Bioscience	RRID: AB_2738426
APC-anti-CD25	Invitrogen	RRID: AB_469366
PE-anti-mouse KLRG1	Invitrogen	RRID: AB_10596642
APC-anti-mouse CD3 ε (145-2C11)	Invitrogen	RRID: AB_469316
APC-Cy7-anti-mouse CD3	BD Bioscience	RRID: AB_1727461
V500-anti-mouse CD90.2 (Thy1.2)	BD Bioscience	RRID: AB_10894013
PE-anti-mouse Siglec-F	BD Bioscience	RRID: AB_394341
PE-CF594-anti-mouse CD127	BD Bioscience	RRID: AB_11153131
BUV395-anti-mouse GATA3	BD Bioscience	RRID: AB_2739241
FITC-anti-mouse Foxp3	Thermo Fisher Scientific	RRID: AB_465243
eFluor450-anti-mouse IL-13	Thermo Fisher Scientific	RRID: AB_11219690
APC-anti-mouse ST2	Thermo Fisher Scientific	RRID: AB_2573301
Alexa Fluor 647-anti-NF κ B p65	Cell Signaling Technology	RRID: AB_2797670
Alexa Fluor 488-anti-NFAT1	Cell Signaling Technology	RRID: AB_2798450
PE- Phospho-CREB (Ser133)	Cell Signaling Technology	RRID: AB_2798432

(Continued on next page)

Continued

REAGENT or RESOURCE	SOURCE	IDENTIFIER
Bacterial and Virus Strains		
<i>Nippostrongylus brasiliensis</i>	Huang et al., 2015	N/A, generated in house
Chemicals, Peptides, and Recombinant Proteins		
Recombinant mouse IL-7	R&D systems	407-ML
Recombinant mouse IL-33	R&D systems	3626-ML
Recombinant mouse IL-33	Biolegend	580508
Rat CGRP	R&D systems	1161
Rat Neuromedin U	R&D systems	1917
666-15	R&D systems	5661
BAY11-7082	Sigma-Aldrich	B5556
SB203580	Sigma-Aldrich	S8307
PD98059	Sigma-Aldrich	P215
N6,2'-O-Dibutyryladenosine 3',5'-cyclic monophosphate sodium salt	Sigma-Aldrich	D0260
YM-254890	Wako Pure Chemical	257-00631
Critical Commercial Assays		
Chromium Single Cell 3' Reagent Kits v2	10X Genomics	PN-120237
NEBNext Ultra RNA Library Prep Kit for Illumina	New England BioLabs	E7530S
NEBNext Poly(A) mRNA Magnetic Isolation Module	New England BioLabs	E7490S
NEBNext Multiplex Oligos for Illumina	New England BioLabs	E7335S
Deposited Data		
Raw and analyzed data	This paper	GEO: GSE131996
ATAC-seq samples for lymphoid cells (related to Figure 2)	Shih et al., 2016	GEO: GSE77695
Experimental Models: Organisms/Strains		
C57BL/6J	The Jackson Laboratory	#000664
B6 (Cg)-Rag2tm1.1Cgn/J (Rag2 ^{-/-})	The Jackson Laboratory	#008448
B6.129S7-Rag1tm1Mom/J (Rag1 ^{-/-})	The Jackson Laboratory	#002216
B6.129S(Cg)-Calcatm1.1(EGFP/HBEGF)Mjz/Mmnc (Calca ^{gfp/gfp})	MMRRC	036773-UNC
Ramp1 ^{-/-}	Kathleen M. Caron	PMID: 25010197
alpha CGRP ^{-/-}	Dr. Anne Luebke	PMID: 10532808
B6;129-Rag2tm1Fwall2rgtm1Rsky/DwlHsd (Rag2 ^{-/-} cg ^{-/-})	ENIVO	#2103F
Software and Algorithms		
TopHat 2.1.0	Trapnell et al., 2012	https://ccb.jhu.edu/software/tophat/index.shtml
Cufflinks 2.2.1	Trapnell et al., 2012	http://cole-trapnell-lab.github.io/cufflinks/
bedtools	Quinlan and Hall, 2010	https://bedtools.readthedocs.io/en/latest/
Bowtie 0.12.8	Langmead et al., 2009	http://bowtie-bio.sourceforge.net/index.shtml
FastUniq	Xu et al., 2012	https://sourceforge.net/projects/fastuniq/
MACS (version 1.4.2)	Zhang et al., 2008	http://liulab.dfci.harvard.edu/MACS/index.html
Hypergeometric Optimization of Motif EnRichment program (HOMER) version 4.9	Heinz et al., 2010	http://homer.ucsd.edu/homer/motif/
R 3.0.1	R Development Core Team, 2018	https://www.r-project.org
Seurat	Macosko et al., 2015	https://satijalab.org/seurat/
Kallisto v 0.43.0	Bray et al., 2016	https://github.com/pachterlab/kallisto
sleuth v 0.29.0	Pimentel et al., 2017	https://github.com/pachterlab/sleuth/
Ingenuity pathway analysis (IPA)	QIAGEN	https://www.qiagenbioinformatics.com/products/ingenuity-pathway-analysis

(Continued on next page)

Continued

REAGENT or RESOURCE	SOURCE	IDENTIFIER
CIMminer	Weinstein et al., 1994	https://discover.nci.nih.gov/cimminer/home.do
The Integrative Genomics Viewer (IGV)	Thorvaldsdóttir et al., 2013	http://software.broadinstitute.org/software/igv/
Partek Genomics Suite	Partek	http://www.partek.com/pgs

LEAD CONTACT AND MATERIALS AVAILABILITY

Further information and requests for resources and reagents should be directed to and will be fulfilled by the Lead Contact, John O’Shea (john.oshea@nih.gov).

EXPERIMENTAL MODEL AND SUBJECT DETAILS

All animal experiments were performed in the AAALAC-accredited animal housing facilities at NIH. All animal studies were performed according to the NIH guidelines for the use and care of live animals and were approved by the Institutional Animal Care and Use Committee of NIAMS. Mice of 6–12 weeks old were used in all experiments. For sample size, see corresponding figure legends.

METHOD DETAILS

Mice

Wild-type C57BL/6J mice, *Rag1*^{-/-} mice, *Rag2*^{-/-} mice were purchased from the Jackson Laboratory. *Rag2*^{-/-}/*gc*^{-/-} mice were purchased from ENVIGO. *Calca*^{gfp/gfp} mice were from MMRRC. *aCGRP*^{-/-} mice were provided by Dr. Anne Luebke (Rochester University) ([Lu et al., 1999](#)).

For generation of bone marrow chimera mice, *Rag2*^{-/-}/*gc*^{-/-} mice were irradiated (600 rads x 2), and were injected intravenously with 5 millions bone marrow cells from either *Ramp1*^{-/-} mice ([Li et al., 2014](#)) or background matched wild-type mice (provided by Kathleen M. Caron). Bone marrow reconstituted mice were placed on antibiotics in drinking water for 2 weeks followed by additional 6 weeks with normal water supply before starting experiment.

Preparation of cell suspensions from tissues

BALF cells were collected from the lung by gently washing with 1 mL of ice cold PBS with 18G plastic cannula and 1 mL syringes. For isolation of cells from lung, mesentery, VAT, small intestine and colon, mice were perfused with 20 mL of PBS for the remove of blood from tissues. The isolated lungs, mesentery and VAT were cut into several small pieces, then were placed in RPMI-1640 containing 2% (vol/vol) FCS (Thermo Fisher Scientific), 50 µg/mL Liberase TM (Roche, 05401127001), 10 µg/mL DNase I (Sigma-Aldrich, DN25) (4 mL per mouse), and incubated for 45 min at 37°C. After that, tissues were further proceeded with the gentleMACS Dissociators (Miltenyi) using gentleMACS C Tubes (Miltenyi), then all cell suspensions were passed 70 µm cell strainers, and then cell strainers were washed twice with PBS to recover cells. Small intestines and colons were harvested and the contents were emptied. Peyer’s patches were removed and then the intestines were opened longitudinally, cut into small pieces and shaken at 37°C for 30 min in HEPES media containing 5 mM EDTA to dissociate intraepithelial cells. The remained fragments were washed twice with HBSS and then were digested at 37°C for 45 min in HBSS media containing 250 µg/mL Liberase TL (Roche, 5401020001) and 10 µg/mL DNase I. The digested tissues were passed 70 µm cell strainers, and then cell strainers were washed twice with PBS to recover cells. The total single cell suspension was enriched with 30% Percoll (GE Healthcare) by centrifugation at 400 g for 20 min, and isolated cells were washed twice before further analysis.

Flow cytometry

Lung ILC2s were identified as lineage markers (CD3ε, CD4, CD8α, CD19, CD11c, CD11b, γδTCR, FcεR1, Gr1, DX5, Ter119) and additional markers as indicated in figure legends. Eosinophils were identified as Siglec-F⁻ CD11b⁺ CD11c⁻ cells. All cells were incubated with anti-CD16/CD32 (2.4G2) to block non-antigen-specific binding of immunoglobulins to the Fcγ receptors before being stained with the appropriate antibodies. For Live/Dead staining, Zombie Violet Fixable Viability Kit (Biolegend) was used. For staining of intracellular cytokines and transcription factors, cells were fixed and permeabilized with Fixation Buffer (Biolegend) or Foxp3 staining buffer (Thermo Fisher Scientific) according to the manufacturer’s instructions. Data were acquired on a FACSCanto II (BD Biosciences) or LSR Fortessa (BD Biosciences) and were analyzed with FlowJo software (Tree Star).

In vitro ILC2 culture

For purification of ILC2s from lung of wild-type mice, lung cells were stained with biotin conjugated anti-lineage markers (CD8α, CD19, CD11c, CD11b, γδTCR, FcεR1, Gr1, DX5, Ter119) and anti-Biotin MicroBeads (Miltenyi Biotec #130-090-485), followed by sorting lineage negative cells by MACS manual separator (Miltenyi). Lineage negative cells were further stained with fluorochrome conjugated antibodies against CD3ε, TCRβ, Thy1, CD127, and KLRG1 together with APC-R700 Streptavidin (BD Biosciences), followed by

sorting ILC2s ($\text{Lin}^- \text{CD3}\varepsilon^- \text{TCR}\beta^- \text{Thy}1^+ \text{CD127}^+$ KLRG1 $^+$) on FACS Aria IIIu or Aria Fusion cell sorter (BD Bioscience). Lung ILC2s were sorted into 96-well plates at the density of 10,000 cells per well and were cultured in 10% RPMI (RPMI1640 medium (Thermo Fisher Scientific) containing 10% (vol/vol) FCS, 50 μM 2-mercaptoethanol (Sigma-Aldrich), 100 U/mL penicillin and 100 $\mu\text{g}/\text{mL}$ streptomycin (Thermo Fisher Scientific) in the presence of 100 U/mL of IL-2 and 10 ng/mL of IL-7. After 2 to 4 weeks, IL-2 and IL-7 were removed from ILC2 culture and additionally cultured for 4 h before use for further analysis. For cytokine production and cell proliferation assays, lung ILC2s were seeded into 96-well round-bottomed tissue culture plates at the density of 5,000 cells per well. For bulk mRNA-seq, lung ILC2s were seeded at the density of 30,000 cells per well. For ATAC-seq, lung ILC2s were seeded at the density of 10,000 cells per well. Cells were cultured in 200 to 300 μL of 10% RPMI with various stimulants, including IL-33 (10 ng/mL), NMU (10 ng/mL), CGRP (10 ng/mL), and Dibutyryl-cAMP (100 μM) in the presence or absence of chemical inhibitors, YM-254890 (10 μM), 666-15 (1 μM), BAY11-7082 (10 μM), SB203580 (10 μM), and PD98059 (10 μM). For intracellular cytokine staining, GolgiPlug (Brefeldin A) (BD Biosciences) was added into the culture from the beginning (4 h stimulation). Production of cytokines in culture supernatant was measured by LEGENDplex Mouse Th Cytokine Panel (Biolegend, #740005) after 5 days culture. Cell proliferation was assessed by trypan blue staining of cells after 5 days culture, or by BrdU uptake of cells cultured for 24 h, followed by addition of 10 μM BrdU for 1.5 h, then detection of incorporated BrdU by flow cytometry according to the manufacturer's instructions (BD Biosciences, #552598).

Nippostrongylus brasiliensis infection

Mice were given subcutaneous injection of 300 or 500 infective third-stage *N. brasiliensis* larvae as described previously (Huang et al., 2015). Worm burden in small intestines were measured on day 7 or 9. Lung cells were harvested on day 2, 5, 9 and 14 after infection for scRNA-seq and bulk mRNA-seq. Before cell sorting, we confirmed comparable viability of cells for all time points tested (93% - 95%).

IL-33-mediated pulmonary inflammation *in vivo*

Mice were anesthetized with isoflurane and treated intranasally with 30 μL of IL-33 (500 ng per mouse) with or without CGRP (1 μg per mouse) in PBS for consecutive 4 days. Treated mice were analyzed 1 day after last administration.

Single-cell RNA sequencing (scRNA-seq)

Freshly sorted ILCs and Th cells (13,000 cells each, cell viability > 98%) were encapsulated into droplets, and libraries were prepared using Chromium Single Cell 3' Reagent Kits v2 according to manufacturer's protocol (10X Genomics). The generated scRNA-seq libraries were sequenced using a 50 cycle (paired-end reads) with a HiSeq 3000 (Illumina).

Bulk mRNA sequencing

Approximately 20,000–50,000 cells (cell viability > 98%) freshly sorted from mice or stimulated with various conditions *in vitro* were lysed with TRIzol (Life Technologies) and total RNAs were extracted using Direct-zol RNA MicroPrep (Zymo Research). Total RNAs were subsequently processed to generate an mRNA-seq library using a NEBNext Poly(A) mRNA Magnetic Isolation Module (NEB, E7490S), NEBNext Ultra RNA Library Prep Kit for Illumina (NEB, E7530S) and NEBNext Multiplex Oligos for Illumina (Index Primers Set 1) (NEB, E7335S) according to protocol. The libraries were sequenced for 50 cycles (single read) with a HiSeq 3000 (Illumina).

FastATAC sequencing

FastATAC-seq was performed according to a published protocol (Corces et al., 2016) with minor modification. Ten thousand cells were pelleted and washed with 50 μL 1 \times PBS. After pelleting the nuclei by centrifuging at 500 \times g for 10 min, the pellets were re-suspended in 50 μL transposase mixture (25 μl of 2x TD buffer, 2.5 μl of TDE1, 0.5 μl of 1% digitonin, 22 μl of nuclease-free water) (#FC-121-1030, Illumina; #G9441, Promega). The reaction was incubated at 37°C with shaking at 300 rpm for 30 min. The fragmented DNAs were then purified using a QIAGEN MinElute kit and amplified with 10 or 11 cycles of PCR based on the amplification curve. Once the libraries were purified using a QIAGEN PCR cleanup kit, they were further sequenced for 50 cycles (paired-end reads) on a HiSeq 3000 (Illumina).

Imagestream

Cells stained for DAPI (CST, #4083), anti-NFAT1-AF488, anti-NF-kB p65- AF647, and anti-CD45- PE/Cy7 were run on an ImageStreamXMKII (Ammis, Seattle, WA) 2 camera imaging flow cytometer at 60X magnification using INSPIRE software. DAPI was detected in channel 7 with a 405 laser power of 30 mW, anti-NFAT1-AF488 was detected in channel 2 with a 488 laser power of 200 mW, anti-CREB -PE, and anti-CD45- PE/Cy7 were detected in channels 3 and 6, respectively, at a 561 laser power of 100 mW, and anti-NF-kB p65- AF647 was detected in channel 11 at a laser power of 150 mW. The 758 laser was turned off for these experiments. 5000 single, in focus cells were acquired. Single color controls were acquired with the Brightfield and 758 lasers off. IDEAS software (Ammis, Seattle, WA) was used to create a compensation matrix and analyze data. Cells with nuclei which were in focus were gated on a histogram of channel 7 Gradient RMS (root mean square). Next, single cells having focused nuclei were gated on an Area_Brightfield versus Aspect Ratio_Brightfield dot plot. DAPI-positive and CD45-positive cells were gated on an Intensity_CD45 versus Intensity_DAPI dot plot gated on single cells with focused nuclei. All subsequent plots were gated on DAPI-positive and CD45-positive cells. DAPI-positive and NFAT1-positive cells were gated on an Intensity_DAPI versus

Intensity_NFAT1 dot plot. DAPI-positive and NF- κ B p65 -positive cells were gated on an Intensity_DAPI versus Intensity_NF- κ B p65 dot plot. The Similarity feature, which is a pixel by pixel comparison of the two images, was created to measure co-localization of NFAT1 and NF- κ B p65, respectively, with the nucleus.

Measurement of cytokines and cAMP

Cytokine concentrations in BALF and supernatant of *in vitro* ILC2 cultures were analyzed by the LegendPlex Mouse Th Cytokine Panel (13-plex) (BioLegend) on a FACS Cant II (BD Biosciences) according to the manufacturer's instructions. For cAMP measurement, 40,000 of ILC2s were stimulated with a variety of stimuli as indicated above, followed by lysis of cells with 50 μ L of lysis buffer (Cell signaling technology, 9803) and measurement of cAMP concentration using Cyclic AMP XP® Chemiluminescent Assay Kit (Cell signaling technology, 8019S). Relative Light Units (RLU) at 425nm were measured by Multimode Microplate Reader (TriStar² LB942).

Histological analysis

Lungs were fixed for at least 24 h with 10% formalin (Sigma-Aldrich, #HT5012) and were embedded in paraffin. Cross-sectional lung tissues were stained with Periodic acid-Schiff (PAS) or hematoxylin and eosin. Pathological score was evaluated by an observer masked to treatment group for the following parameters: peribronchiolar inflammation and cuffing (0–4), perivascular inflammation and cuffing (0–4), goblet cell hyperplasia (0–4) and interstitial infiltrate (0–3).

Immunofluorescence microscopy

Lung was fixed in 2% PFA for 4 h on ice and incubated in 30% sucrose at 4°C overnight, followed by embedding in OCT (Leica) for cryocutting. 8- μ m tissue slices on slides were washed 3 x in ice-cold PBS, blocked in 10% donkey serum in PBS and stained with: hamster anti-CD3ε-APC (145-2C11, eBioscience), hamster anti-KLRG1-PE (2F1, eBioscience). Nuclei were counterstained with DAPI (Thermo Fisher Scientific). Images were captured with an inverted Nikon Eclipse Ti microscope (Nikon).

QUANTIFICATION AND STATISTICAL ANALYSIS

Bulk mRNA-seq analysis

Raw sequencing data were processed with CASAVA 1.8.2 (Illumina; ([Bentley et al., 2008](#))) to generate FastQ files. Sequence reads were mapped onto mouse genome build mm10 using TopHat 2.1.0 ([Trapnell et al., 2012](#)). Gene expression values (FPKM; fragments per kilobase exon per million mapped reads) were calculated with Cufflinks 2.2.1 ([Trapnell et al., 2012](#)). BigWig tracks were generated from Bam files and converted into bedGraph format using bedtools ([Quinlan and Hall, 2010](#)). These were further reformatted with the UCSC tool bedGraphToBigWig. Pathway analysis and prediction of upstream gene were performed with Ingenuity pathway analysis (IPA). Scatterplot was created with Partek Genomics Suite (Partech). The Pearson correlation analysis was done by corr() function in R 3.0.1 ([R Development Core Team, 2018](#)) and the heatmap and clustering tree was plotted by “pheatmap” package in R using clustering method “ward.” The heatmap showing gene expression was created with CIMminer ([Weinstein et al., 1994](#)).

ATAC-seq analysis

FastATAC-seq reads from two biological replicates for each sample were mapped to the mouse genome (mm9 assembly) using Bowtie 0.12.8 ([Langmead et al., 2009](#)). In all cases, redundant reads were removed using FastUniq ([Xu et al., 2012](#)), and customized Python scripts were used to calculate the fragment length of each pair of uniquely mapped paired-end (PE) reads. The fragment sizes distribute similar to previously published data (data not shown). Only one mapped read to each unique region of the genome that was less than 175 bp was kept and used in peak calling. Regions of open chromatin were identified by MACS (version 1.4.2) ([Zhang et al., 2008](#)) using a p value threshold of 1×10^{-5} . Only regions called in both replicates were used in downstream analysis. Peak annotation and motif analysis were performed with the Hypergeometric Optimization of Motif EnRichment program (HOMER) version 4.9 ([Heinz et al., 2010](#)) using the “annotatePeaks.pl peak_file mm9 -size 1000 -hist 40 -ghist” and “findMotifsGenome.pl peak_file mm9 motif_folder -size given -preparsedDir tmp 2>out.” The heatmap were generated by “pheatmap” package in R 3.0.1 ([R Development Core Team, 2018](#)).

scRNA-seq analysis

Sequence reads from all samples were processed and aggregated using Cell Ranger. Aggregated data was further analyzed by Seurat ([Macosko et al., 2015](#)). Specifically, we log-normalized the expression matrix, regressed the data against the total number of UMI's detected per cell, performed PCA analysis, used PCA dimensions 1-10 to find clusters, and finally found marker genes for these clusters. We visualized single cell gene-expression as tSNE overlays, marker gene heatmaps, and violin plots. We used the normalized expression matrix, tSNE coordinates, and clustering produced by Seurat for the transcription module analysis described below.

Analyzing transcriptional modules

To explore cytokine-induced transcriptional modules in our scRNA-seq data, we first defined modules by calling differentially expressed genes in our bulk samples, and then scored each single cell based on their expression of these genes. Specifically, we used kallisto v 0.43.0 to quantify abundance ([Bray et al., 2016](#)) and sleuth v 0.29.0 ([Pimentel et al., 2017](#)) to define differentially

expressed genes ($q\text{-value} < 0.05$; fold change $>= 1.5$; higher than 10 TPM expression in at least one sample) in bulk samples treated with IL-33, NMU, CGRP, or cAMP compared to no stimulation. Next, we row-normalized the single cell gene expression matrix produced by Seurat to obtain Z-scores. To calculate a module score for each single cell, we added the Z-scores of upregulated genes and subtracted those of downregulated genes, then normalized by the total number of module genes. To partially overcome the dropout artifact of 10X sequencing, we only considered module genes that expressed at least 300 TPM in at least one bulk sample. In our hands, genes expressed at this level are detected by 10X sequencing in approximately 50% of single cells. We performed module analysis using ILC cells with detectable *Gata3* expression.

Statistical analysis

Statistical significance was assessed with non-paired two-tailed Student's t test.

DATA AND CODE AVAILABILITY

The data discussed in this publication have been deposited in the NCBI Gene Expression Omnibus and are accessible through accession number GEO: GSE131996.